SEMIANALYTIC MODELS OF TWO-PHASE DISK WINDS IN ACTIVE GALACTIC NUCLEI WITH COMBINED HYDROMAGNETIC AND RADIATIVE DRIVING

John E. Everett

Department of Astronomy and Astrophysics, University of Chicago, 5640 S. Ellis Avenue, Chicago, IL 60637

Submitted to ApJ

ABSTRACT

We present a semianalytic model of steady-state magnetically and radiatively driven disk outflows in Active Galactic Nuclei (AGNs) consisting of a continuous wind with embedded clouds. The continuous outflow is launched from the disk surface as a centrifugally driven wind, whereas the clouds are uplifted from the disk by the ram pressure of the continuous outflow. The inner regions of the outflow shield the outer portions from the strong ionizing central continuum, enabling gas in the outer regions to be radiatively accelerated. In this paper, we describe the model in detail, outline the tests used to verify its accuracy, and then compare it to other outflow models already in use, showing that some previous AGN wind simulations do not consider radiative transfer in the detail necessary for accurate modeling. We also perform a comprehensive parameter study to explore the dependence of the continuous wind properties on the relevant physical parameters. We find that the introduction of clouds has a significant impact on the geometry, density, and terminal velocities of the continuous wind: in particular, changes of up to 50% in the wind velocity can be directly attributed to the effect of clouds. Within this survey, line driving is often the dominant acceleration mechanism for clouds, owing to their small volume filling factor, which yields an overall low cloud opacity. Continuum driving can also become important for dusty clouds. For the continuous wind alone, we find that radiative acceleration can have a significant impact on both the terminal velocities and the kinematics near the surface of the disk. However, unlike the clouds, the radiative acceleration of the continuous wind comes largely from continuum opacities, not from line driving as in some previous models. Line driving produces comparable acceleration only for parts of the wind far from the central source, where the ionization state of the gas drops due to the lower incident flux. When the winds are dusty, their terminal velocities change by approximately 20% to 30% (depending on the type of dust) over pure centrifugally-driven outflows.

1. INTRODUCTION

Active Galactic Nuclei (AGNs) often declare themselves boisterously to observers: well-known for their incredibly bright nuclei, they can also display emission line widths of up to several thousand km s^{-1}, and absorption lines in the optical, UV, and X-ray, with blueshifts up to 60,000 km s^{-1}. They do not yet, however, communicate as well with theorists: we lack a physical picture of the geometry and kinematics of gas in the core of AGNs. Researchers agree that AGNs house supermassive black holes, but other components of the theoretical picture spark heated debate. The payoff for building a successful model of the geometry and kinematics of gas in AGNs is very high: not only will we gain understanding of how AGNs work, and insight into the almost ubiquitous phenomenon of accretion and the physics of black holes, but we may also learn about how galaxies evolve (e.g., Blandford 2001).

In the absence of any well agreed-upon theoretical model, researchers have put together a phenomenological picture of the structure of AGN, called the "Unification Model"(Antonucci 1993; Urry & Padovani 1995). As commonly cited, this paradigm consists of a supermassive black hole with an accretion disk, as well as a coplanar "torus" of gas and dust that orbits near the outskirts of the accretion disk; the location, composition, and dimensions of the torus remain unknown. Gas, commonly modeled as clouds and postulated to exist above the accretion disk, produces both the broad emission lines (within the Broad Emission Line Region, or BELR) and, further from the central source, the narrow emission lines. This model has proven itself useful through its explanation of the difference between AGNs that contain only narrow emission lines, and those that contain both broad and narrow lines: if the AGN is oriented so that our line of sight intersects the torus, it obscures the broad lines region, and we see only narrow emission lines. In recent years, models that further elucidate the geometry and kinematics of gas in the unification model have also been proposed (e.g., Elvis 2000; Ganguly et al. 2001); although these models cite the need for such mechanisms as radiative acceleration, they remain chiefly empirical.

Observational hints are now appearing that the unified, "inclination angle" paradigm for AGNs may not work in all objects. In fact, relatively few AGNs have been used as proof of this unification model (Axon 2001). In addition, inclination-angle independent measures of various AGNs seem to show variations which are not in agreement with the unified model (Weymann 2002). Recent X-ray observations of AGNs seem to show objects that have large X-ray absorbing columns, and yet have broad optical emission lines, while other sources with only narrow optical emission lines have no apparent X-ray absorption (Pappa et al. 2001). Thus, the empirical models of gas distribution in the central regions of AGNs might not be as widely applicable as previously thought. At the root of this difficulty lies the fact that we are still quite ignorant of what forces dominate in different parts of the nuclei of active galaxies, or what forces may dominate in different AGNs.

To solve this problem, and develop consistent dynamical models of AGNs, researchers have appealed to two major sources of acceleration: magnetohydrodynamic driving of clouds (e.g., Emmering et al. 1992; Bottorff et al. 1997), and radiative acceleration of continuous winds (e.g., Murray et al. 1995; Proga et al. 2000). One can also see in the above very short summary that the field is somewhat divided on whether we are watching continuous outflows or "clumpy" outflows [however, the continuous wind simulations of Proga et al. (2000) can produce condensations that may be the source of a multiphase medium]. Both of these types of models have had successes in modeling AGN observations; for instance, both the magnetohydrodynamic model (Bottorff et al. 1997) and the radiative acceleration model (Murray & Chiang 1997) have reproduced the observed single-peak broad emission lines observed in AGNs. Since these models have fit the basic observational traits of AGNs, there seems to be no clear way to select which physics may be dominant in which AGNs, and we are left with two very different outflow scenarios. The challenge remains, therefore, to develop tools that can distinguish between these models and that will allow us to test for the presence of individual forces or components. A general model seems necessary: one that self-consistently handles all of the elements that have been previously proposed, so that we can systematically test one inclusive model against the observations. Such a model may help us gain insight into how AGN winds work, how gas is distributed in the cores of AGNs, and may aid in testing theories about accretion disks and AGN evolution.

This paper presents such a tool, including all of the above mentioned elements and their interactions (such as the interplay between magnetic forces and radiative driving, and the drag forces between the continuous wind and the clouds) to provide a physically self-consistent "platform" from which to test all of the different components, together.

This paper outlines our motivation for such a model, defines the particular construction we have chosen, and introduces a parameter survey to aid intuition of how the included processes interact.

The paper begins with an outline of past models in §2, ending with an overview of our model. In §3, we describe the various components of our model, and in §4 we present early results from our calculations, showing the dependences of wind velocities and densities on various input parameters. We summarize our findings in §5.

2. AGN OUTFLOW MODELS: THE CURRENT STATE OF THE ART

This section summarizes previously proposed models; this may be useful, as our work builds on the results of past work, including elements from many of the models mentioned.

2.1. "Clumpy" Winds

Many of the models used today to reproduce AGN observations are photoionization codes that invoke discrete clouds (e.g., Hamann et al. 2001; de Kool et al. 2001). In many cases, no dynamical information is input to the model; these winds are modeled as clumps of gas that intercept the radiation from the central source (see, however, Chelouche & Netzer 1999). These cloud models have an extensive history in fitting AGN winds (see Netzer 1990): for instance, they have been used to explain how both high and low ionization lines occur together (using optically thick clouds) with similar line profiles. They are also attractive since such inhomogeneous winds predict much smaller mass outflow rates compared to continuous winds. In addition, continuous wind simulations seem unstable to producing density inhomogeneities, making clouds a somewhat ubiquitous component in AGN wind models.

However, there has been some doubt cast on this picture recently, as high-resolution analysis of emission line profiles seems to suggest many more clouds than specified by photoionization analysis (Arav et al. 1997, 1998; Dietrich et al. 1999). As a result, some researchers have turned to continuous wind models instead of discrete clouds. Another problem with the cloud models is that these clouds must be confined in some way in order to retain their distinct identities, and finding a confining mechanism has remained a difficult task. Some researchers have called on magnetic confinement (Rees 1987), but others claim that magnetic confinement has never been proven to work. The response to this argument has typically been that since the solar wind confines clouds within the magnetic structure of its outflow, perhaps it is possible for an AGN outflow to do the same (Weymann 2002).

2.2. Radiative Acceleration of Continuous Winds

As an alternative to clumpy winds, some researchers have developed continuous wind models, usually powered by radiative acceleration. Radiative acceleration is the force felt by atoms due to momentum conservation: atoms de-excite isotropically after absorbing radially (thus, anisotropically) streaming photons from the central source. Since the late 1970's, radiative acceleration has been a popular mechanism for explaining stellar winds (e.g., Castor, Abbott, & Klein 1975; Abbott 1978), and has become an attractive candidate for AGN winds (e.g., Arav et al. 1994; Murray et al. 1995; Proga et al. 2000) because we know that there is an intense radiation field in AGNs. Therefore, it seems very likely that radiative acceleration should be important somewhere within the outflow. In addition, radiative acceleration calculations have shown that the observed terminal outflow velocities can be achieved (Murray et al. 1995, hereafter, MCGV95). Researchers have even been able to reproduce the characteristic AGNs single-peaked broad line profiles using radiatively accelerated, continuous winds (Murray & Chiang 1997). There have also been several observational hints that radiative acceleration is an important force in AGN: for instance, the dependence of absorber terminal velocity on AGN luminosity (Laor & Brandt 2002) and the phenomenon of spectral absorption "line locking" (Arav 1996).

However, radiative acceleration becomes important only with the right balance of UV and X-ray radiation: too much flux in the X-ray band can strip atoms of their electrons, leaving many fewer line transitions for atoms to absorb and accelerate with (Proga et al. 2002). But if one decreases the continuum enough to leave the atoms intact, the UV

radiation absorbed by the atomic transitions also decreases. In order to deliver the right amount of radiation to their winds, MCGV95 call upon a modified MF87 spectrum in the X-ray band to mirror radio quiet quasars: whereas Mathews & Ferland (1987, hereafter MF87) has an α_{OX} of 1.4 and a power-law slope of -0.7 above 0.4 keV, MCGV95 call upon an α_{OX} of 1.5 and a power-law slope of -1 throughout the X-ray band. (α_{OX} is the spectral index that describes the power law slope connecting the continuum at 2500 Åand 2 keV.) MCGV95 also utilize a gas shield to attenuate that continuum. As this shield is crucial to their model, a self-consistent explanation for the presence of that shield would be a very important element in any AGN model.

2.3. *Magnetic Acceleration of Continuous Winds or Clouds*

The use of magnetic stresses as a possible source of acceleration and collimation of AGN winds stretches back to Blandford & Payne (1982, hereafter BP82), and since then has been developed by other researchers (e.g., Emmering et al. 1992; Königl & Kartje 1994; Bottorff et al. 1997; Kartje, Königl, & Elitzur 1999). The primary reason that such magnetic field models are attractive is that not only could they help form the collimated jets that we observe at large scales, but more importantly, they transport angular momentum from the accretion disk, allowing matter to fall towards the central source. The classic description of this model involves visualizing the magnetic field lines as wires, and gas elements as beads on that wire (assuming that the gas and the field are well-coupled, which is a good approximation if the gas is well ionized). If the magnetic field meets the disk at an angle $\leq 30°$ to the vertical, then due to centrifugal forces, the gas "sees" a potential drop along the magnetic field line. Because of this potential drop, the gas launches from the accretion disk, moving along the field lines. Thus a wind moves upward from the disk, and will later be collimated by the same magnetic field lines. This collimation occurs due to the increase in importance of the matter's inertia relative to the magnetic field strength: as the wind rises, the magnetic field amplitude drops, and the rotational motion of the gas (retained from the disk) starts to dominate the gas streamlines, twisting the magnetic field into a coil-like shape that confines the outflow. The self-contained launching and collimation mechanism in this theory along with its possible role in helping matter accrete make this one of the most appealing, generally-applicable models to a wide variety of disk/wind systems (Livio 1999).

In addition to explaining collimated jets and helping matter accrete in the disk, magnetic winds may be valuable for AGN models in that they can also supply magnetic pressure and confine clouds embedded in the wind. Also, radiatively accelerated wind models will have difficulty launching a wind in heavily-shielded (or otherwise very low luminosity) regions of the outflow, which could be the case near the surface of the accretion disk. Magnetic stresses could lift the wind up to a starting point where the radiative acceleration would become effective, regardless of the shielding or the luminosity of the AGN (a very luminous accretion disk could also play an important role in wind launching, however). Finally, magnetic winds most easily accelerate gas that is highly ionized and could thus launch an unshielded wind; in comparison, radiative acceleration drops when the gas is highly ionized since such gas would not have a large array of lines to absorb the photons necessary to accelerate the gas. The magnetically launched wind could then provide a gas shield for winds farther removed from the central source.

Magnetic wind models are also not without detractors: some researchers argue that the required, relatively ordered magnetic field structure does not exist, and that magnetic pressure is not adequate to confine gas clouds (e.g., MCGV95). Others argue that magnetic fields represent "extra forces" that are not yet required in the face of radiative acceleration models (Weymann 2002).

In addition, past models of magnetically accelerated winds have not fully addressed the difficulties of mixing a magnetocentrifugal wind with radiative acceleration, or with combining a continuous wind with embedded clouds. Königl & Kartje (1994, hereafter KK94) contained an approximate, schematic formula for radiative acceleration due to dust; they did not attempt to include a detailed photoionization treatment, and did not self-consistently include the radiative acceleration within the framework of the self-similar MHD wind model. Also, Emmering et al. (1992) analyzed AGN cloud dynamics by using a continuous wind model in which the magnetic field structure was fixed. Very little previous work has been done on a model that includes both a continuous wind and explicit clouds, the interaction between them (pressure equilibrium and ram pressure), or the more large-scale problem of the self-consistent solution of the magnetic and radiative acceleration forces (see, however, Proga 2002).

Each of the above models, with their respective geometries and forces, have duplicated some aspect of AGN observations: some have matched observed column densities, and in the case of dynamical models, have even reproduced AGN emission line profiles (Bottorff et al. 1997; Murray & Chiang 1997). So far, the different dynamical models seem to give very similar observational predictions since they both result in somewhat similar kinematics. This has led to a serious difficulty: there is no easy way to discriminate between these possibilities and learn what is really powering AGN winds. It may be important, therefore, to develop models that can take these various forces into account and determine what differences we can observe to discriminate among them, or to determine the interplay of those forces within any given AGN.

2.4. *Self-Consistent Integrative Models*

We have developed a self-consistent model of Active Galactic Nuclei winds, integrating all of the above forces within the same program, and also taking account of their interactions. This semianalytic model includes magnetic acceleration and radiative acceleration of both a continuous wind and clouds, as well as the drag forces between the clouds and the wind. In addition, through the use of the photoionization simulation program Cloudy (version 96 Beta 4; Ferland 2001), we have included a detailed treatment of radiative transfer.

A schematic flow chart (see Fig. 1) gives a quick overview of the model procedure: there are seven different programs at work within that structure. We start with a self-similar magnetohydrodynamic model that gives the pure MHD wind solution, then simulate the photoionization balance of that wind, and use the resultant ionization balance to derive the radiative acceleration of the wind and the embedded clouds. Next, we input the radiative acceleration of the wind back into the self-similar magnetohydrodynamic model, modifying the structure of the wind. We also input into the self-similar model the drag forces felt by the continuous wind due to the motion of the embedded clouds. We then repeat the process again, simulating the photoionization of that modified wind and recalculating the radiative acceleration terms. We typically iterate three to five times to converge to a final equilibrium solution.
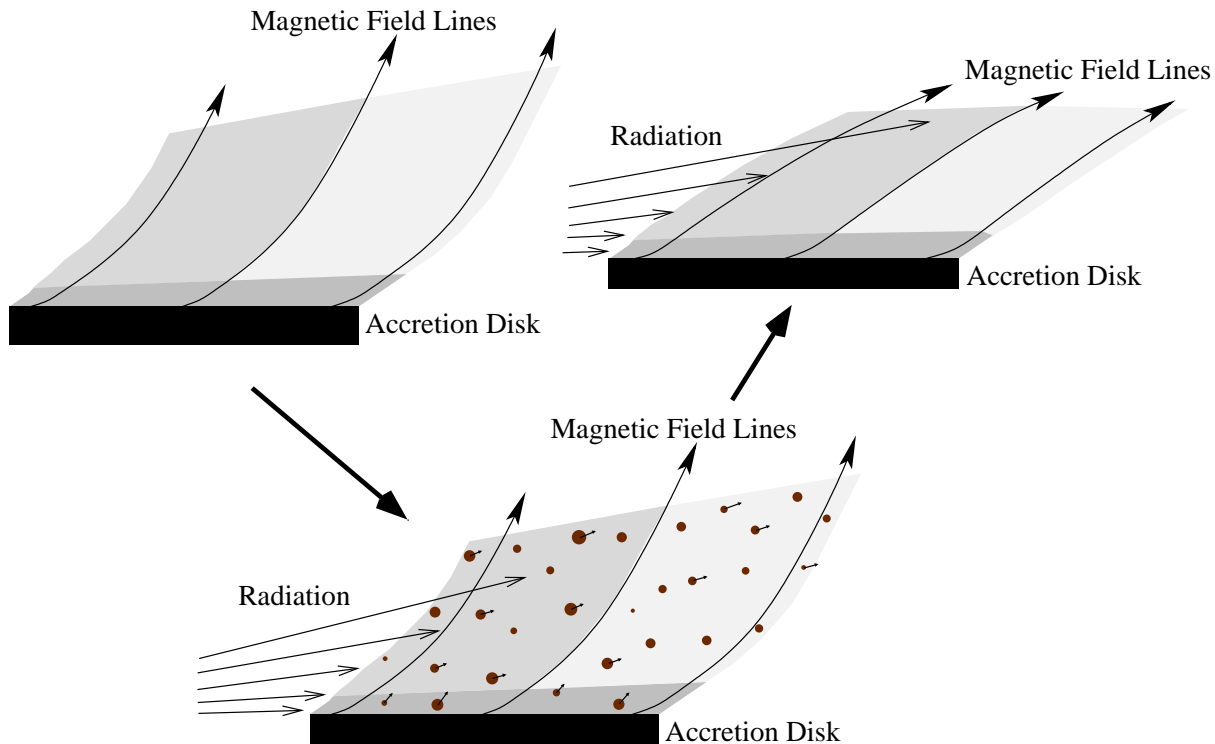

FIG. 1.— A schematic of the iterative scheme of our AGN wind model. We represent a single iteration of the model, moving counter-clockwise around the above diagram. The model starts by solving the self-similar MHD equations for the structure of a centrifugally driven wind (*upper left*). Next, we use photoionization simulations to determine the ionization state of the gas, and then we use those results to calculate the radiative acceleration of the wind. We also add clouds to the wind: clouds which are magnetically confined and radiatively accelerated, and interact with the wind through drag forces only (*lower center*). We then apply the output from the radiative acceleration calculation to the self-similar MHD wind, using radiative acceleration to decrease gravity in a height-dependent way. This modifies the wind's structure, taking into account the radiative forces (*upper right*). With the arrows, we denote the velocity vectors of individual clouds; near the disk, where the shielding column to the central source is high, the clouds feel predominantly the drag of the wind, and are launched from the disk. Further up in the wind, the column of gas in the wind decreases as the wind accelerates, the clouds intercept more radiation, and radiative acceleration becomes the dominant force.

Since we "initialize" the wind with a self-similar magnetohydrodynamic flow, we are building in assumptions similar to that of previous MHD models (e.g., Emmering et al. 1992). The assumption of self-similarity is critical in enabling us to model the magnetocentrifugal wind. However, at the core of the self-similar model is the assumption that variables scale via proscribed power-laws; for instance, the spherical radial velocities all must scale as $R^{-1/2}$, where R is the spherical radial coordinate. We recognize this assumption by limiting our model to be strictly local, i.e., the calculation is carried out and applicable only for a limited range of launching radii $\Delta r \ll r_{\rm wind}$. This limit must also be imposed because of the extreme sensitivity of radiative acceleration to ionization conditions, which means that the calculations must by nature be local to where the photoionization results are obtained. Such local wind models seem, however, very apropos to current AGN theories: researchers have postulated that the wind is indeed outflowing in small sectors (e.g., Emmering et al. 1992; de Kool & Begelman 1995; Arav et al. 1998), and such outflows may have even been observed (Arav 1996). This is interesting as such an outflow does not require the large scale, ordered magnetic fields that may be difficult for an AGN accretion disk to produce. It is important, however, to keep this limitation in mind: this model and its results apply to local sectors, or flux tubes, of the outflowing wind.

Now that we have described the basics of our model, it may be instructive to compare and contrast it to the recent wind model examined in Proga (2002), where the combination of magnetic and radiative forces in disk winds is also investigated. Proga (2002) concentrates on numerical simulations of time-dependent winds with line driving and magnetic forces. These numerical simulations allow large-scale models of outflows that are very valuable in understanding global

wind structures in many different astrophysical contexts. In contrast, the wind solutions presented here are much more localized, as mentioned above. However, as we will find in §4.2, this limitation is very important to accurately calculating the radiation force on the wind, since we employ detailed photoionization simulations. We have chosen our model setup for its accuracy and flexibility in radiative acceleration modeling; using Cloudy enables computations not only of line driving but continuum driving, and allows us the freedom to include dust and easily vary the incident spectrum. In addition, it is important to realize that the magnetic winds produced in Proga (2002) are not magnetocentrifugal (BP82) outflows, as are the semianalytic winds that we present. Further, our models are steady-state, and not time-dependent. We also explicitly include confined clouds, while Proga (2002) only simulates continuous winds. Finally, semi-analytic, steady-state models allow an exploration of general behaviors through many parameter variations; large-scale numerical simulations can usually vary only a few parameters. In summary, these models cover different facets of the disk-wind problem, yielding valuable, different perspectives on a complicated system.

3. THE TWO-PHASE HYDROMAGNETIC AND RADIATIVE WIND MODEL

In this section, we describe all of the components in our model, and outline the derivation of key equations.

3.1. *Magneto-Centrifugal Self-Similar Wind Solution*

The first part of our model solves the equations of motion for gas in a magnetohydrodynamic (MHD), centrifugally-driven wind that is uplifted, guided, and collimated by a magnetic field.

3.1.1. *Continuous Wind Equations*

To derive the equations governing the continuous wind, we start with the equations of a stationary, axisymmetric magnetohydrodynamic flow in cylindrical coordinates, and utilize the continuity equation, conservation of angular momentum along the flow, and both the radial and vertical momentum equations (much as in BP82 and KK94). We neglect thermal effects in the wind, therefore effectively assuming that the wind starts out supersonic. In deriving the equations of motion, we use the same simplifications as BP82, except for the added complication that energy is not conserved in our system, due to the constant input of radiative energy into the system. In the original formation of BP82, conservation of energy supplied an additional equation which allowed a simplification of their equations of motion to two first order differential equations. Because we lack an energy constraint, we must integrate the equivalent of three first-order differential equations, solving for three parameters simultaneously instead of the two that are solved for in the case of BP82. The detailed setup and derivation of our equations of motion is are given in Appendix A.

We start the integration of the momentum equations by specifying the following initial parameters: the mass loading of the wind (the ratio of mass flux to magnetic flux in the MHD wind, $\kappa \propto \frac{4\pi\rho v_p}{B_p}$, where ρ is the mass density of the wind, v_p is the poloidal velocity of the wind, and B_p is the poloidal magnetic field strength), the specific angular momentum of gas in the wind, and the power-law exponent that describes the change in density with spherical radius, b: $\rho \propto R^{-b}$. We also input, as parameters, the mass of the central black hole, $M_\bullet$, the wind's launch radius on the disk, r_0, and the density at the base of the wind (at r_0), n_0. The program employs a "shooting" algorithm (using the SLATEC routine DNSQ from Powell 1970) to integrate from the critical point (the Alfvén point) to the disk, solving for the height of the critical point above the disk (χ_A) and the slope of the streamline at both the disk and the critical point (ξ'_0 and ξ'_A) by matching the integration results to boundary conditions on the disk. After solving for the position of the Alfvén point, we integrate the equations of motion from the disk to a user-specified height beyond the Alfvén point, calculating the run of velocity, density, and magnetic field along the gas flowlines.

3.1.2. *Testing*

We have tested this code (without radiative acceleration) against the results given in BP82 and have duplicated their results to within 8%. This is fairly close to the previously reported 4% variance in recalculating their models (Safier 1993).

3.2. *Photoionization Simulations of the Wind*

We next use the photoionization code Cloudy (Ferland 2001) to simulate the ionization state of the above MHD wind due to radiation from the central AGN source. We use photoionization simulations both of the continuous wind and the clouds in our model to accurately calculate the radiative acceleration of both components. We can use any central spectrum we wish, although we currently call on the MF87 and MCGV95 spectra for the tests in this paper.

3.2.1. *Photoionization of the Continuous Wind*

Our goal in using Cloudy is to simulate the ionization state of the gas and the radiative acceleration along a streamline within the wind. We specify which streamline by giving Cloudy the distance of the base of that streamline from the central continuum source, as well as the wind's column density between the launch point and the innermost region of the wind. That part of the wind (between the central source and the streamline of interest) acts as a shield for the streamline under consideration.

However, there is a complication to running photoionization simulations for these wind models: in many cases, near the base of the wind, the gas could be optically thick. Programs like Cloudy have an understandably difficult time working

with optically thick models, so when we are in a region of the wind where the shielding column is large enough to yield $\tau_{es} > 1$, we divide (computationally) the wind into a $\tau_{es} \sim 1$ section and a remaining section that we simulate as a pure electron scattering zone. To do this, we compute τ_{es} as follows:

$$\tau_{es} = \sigma_T N_H = \sigma_T \int_{R_{in}}^{R_{out}} n(R)dR, \tag{1}$$

where σ_T is the Thomson cross section, and R is the spherical, radial distance. For the time being, we assume the same scalings as BP82, and set $b = \frac{3}{2}$; other scalings are possible (Contopolous & Lovelace 1994). We then write

$$n(R) = n_0 \left(\frac{R_0}{R} \right)^{\frac{3}{2}}. \tag{2}$$

Substituting that into our expression for τ_{es}, we find

$$\tau_{es} = 2\sigma_T n_0 R_0 \left(1 - \frac{R_{out}}{R_0} \right)^{\frac{1}{2}}. \tag{3}$$

Again, if this $\tau_{es} > 1$, we can only simulate a $\tau_{es} \sim 1$ region in Cloudy, so we solve for the size of the column of gas in front of our streamline that supplies $\tau_{es} = 1$, and pass that part of the wind to Cloudy to simulate. To include the effect of the wind that we cannot have Cloudy simulate (that part of it closer to the central source), we simply attenuate the AGN spectrum by $e^{\tau - 1}$ and pass that spectrum to Cloudy for the start of its calculation. When this program has finished, we record the ionization state of the gas as well as the radiation field at that point in the wind.

3.2.2. *Photoionization of the Clouds*

After simulating the radiative transfer through the wind, to our streamline of interest, we run another set of photoionization simulations to determine the photoionization state of clouds locally in that wind. But there is a complication here: the level of wind shielding in some of our calculations is so high very near the disk that Cloudy cannot simulate the ionization state there. This becomes a complication in the cloud models where we need to have some estimates of the clouds' properties in order to understand their launching. The details of how we define our initial cloud parameters are given in Appendix B.

To keep the cloud parameters consistent with magnetic confinement, the program iterates the Cloudy simulations of the clouds, adjusting the density of the clouds until pressure balance between the clouds and the magnetic pressure of the outside continuous wind is reached, satisfying: $\frac{B_{wind}^2}{8\pi} = n_{cloud}kT_{cloud}$ (the code stops when they are equal to within 5%). When these Cloudy runs are finished, the code outputs the density, ionization structure, and radiation field in the clouds at each point in the wind. With these physical parameters set, we can calculate the radiative acceleration of the clouds and the wind.

3.3. *Radiative Acceleration Calculations*

At this point, we engage a FORTRAN program that uses Cloudy's results for the ionization structure and radiation field to calculate the radiative acceleration felt by the wind and clouds. There are two different kinds of radiative acceleration to consider: continuum acceleration (which includes radiative acceleration on dust) and line acceleration. When we specify the radiative acceleration, it is convenient to refer to $\Gamma(\theta)$

$$\Gamma(\theta) \equiv \frac{a_{radiative}(\theta)}{g}, \tag{4}$$

where $a_{radiative}$ is the acceleration due to radiative forces, and g is the local gravitational acceleration.

3.3.1. *Line and Continuum Acceleration*

In general, for continuum and line acceleration, the radiative acceleration is given by

$$\Gamma = \frac{\frac{n_e \sigma_T F}{\rho c}(M_{cont} + M_{lines})}{\frac{GM_\bullet}{r^2+z^2}}, \tag{5}$$

where F is the incident flux, n_e is the electron density, ρ is the gas density, c is the speed of light, G is the gravitational constant, $M_\bullet$ is the mass of the central black hole, r and z are the radial and vertical distance from the black hole, and M_{lines} & M_{cont} are the "force multipliers" that relate how much the radiative forces on the gas exceed the radiative forces on electrons alone. They are given below in terms of the continuum opacity, χ_ν, and the line opacity, χ_l

$$M_{cont} = \frac{1}{n_e \sigma_T F} \int \chi_\nu F_\nu d\nu, \tag{6}$$

$$M_{lines} = \frac{1}{F} \sum_l F_l \Delta\nu_l \frac{1 - e^{-\eta_l t}}{t}, \tag{7}$$

with

$$\eta_l \equiv \frac{\chi_l}{\sigma_T n_e} \qquad\qquad t \equiv \frac{\sigma_T n_e v_{th}}{\frac{dv_R}{dR}}, \qquad\qquad (8)$$

where ν is the frequency, F_l is the flux in the line at the frequency of line l, v_{th} is the thermal velocity in the acceleration gas, $\Delta\nu_l = \nu v_{th}/c$ is the thermal line width, and η_l compares the opacity of the line (given the ionization state of the gas) to the electron opacity, including all of the atomic physics in the radiative acceleration calculation. The variable t is often called the "effective electron optical depth." This parameter sets line driving apart from all other radiative transfer problems: t encodes the dynamical information of the wind in the radiative acceleration calculation. In standard, stationary radiative transfer problems, one calculates the optical depth in atomic lines based purely on the linear depth and density of the matter. In an accelerating medium, one must also account for the Doppler effect: a certain distance from the position of a line photon's creation, the gas has accelerated to such an extent that, in the rest frame of that downstream gas, the photon's energy has shifted beyond the energy range that can be absorbed by that atomic line. This length is termed the "Sobolev length," and is a key parameter in understanding the dynamics of radiatively driven flows (Sobolev 1958, 1960; Castor 1970; Castor, Abbott, & Klein 1975; Mihalas & Weibel-Mihalas 1999). The parameter t includes the effect of the limiting Sobolev length by multiplying the standard electron optical depth by $v_{th}/\frac{dv_R}{dR}$, which is the length at which a photon has redshifted out of the thermal width of a given line.

We calculate the force multipliers for every point in the wind where we have photoionization simulation results, using the resonance lines given in Verner et al. (1996). Since M_{cont} depends only on the ionization state, as soon as we have photoionization data, we know the continuum force multiplier. We compute M_{line} for a range of values of the parameter t. In the subsequent radiative acceleration calculation, we linearly interpolate both of these tables to evaluate the radiative acceleration, given the local ionization state and the local velocity gradient.

3.3.2. *Dust Acceleration*

To include radiative acceleration due to dust, we simply specify to Cloudy that the gas includes dust (specifying to Cloudy both the type of dust and the gas abundances corresponding to that dust). In our models so far, we have primarily used ISM gas abundances and dust (Mathis, Rumpl, & Nordsieck 1977; Draine & Lee 1984; Martin & Rouleau 1991). We have also found wind solutions for clouds with Orion abundances and dust (the Orion dust differs in the size cutoffs in the grain distribution: whereas the ISM dust has grains of minimum size $a_{\min} = 0.0025$ μm, the Orion dust distribution has $a_{\min} = 0.03$ μm, believed appropriate to a UV-irradiated medium; Baldwin et al. 1991). For the grain type specified, Cloudy then automatically includes the relevant dust opacity in the continuum opacity that we use to calculate the continuum force multiplier.

We include dust in the clouds by default to not only be consistent with previous findings (Everett, Königl, & Arav 2002), but also because the surface of the accretion disk is often envisioned as having a high-temperature corona: in such a corona, dust would be much more likely to survive in the lower-temperature environment of the denser clouds. However, for full generality, the program also allows the user to add dust to the continuous wind to observe the effects of that dust on the outflow. Our parameter survey (see §4.3) includes such models.

Within our model, we are careful to include dust only where the photoionization models allow it to survive. Primarily, this means considering sublimation: for the ISM and Orion dust typically used in these simulations, graphite and silicate dust sublimate at $\sim$1750 K and $\sim$1400 K, respectively. We handle the process of dust sublimation by including dust, automatically, where-ever the user requests it, in our first photoionization simulations; if the dust temperatures rise above the given sublimation temperatures, the program removes dust from the calculation, reruns Cloudy, and does not include dust in any subsequent photoionization simulations downstream in the wind.

3.3.3. *Testing*

We have tested the computation of the force multipliers against Arav et al. (1994), who also calculated the radiative acceleration from photoionization simulations. Figure 2 compares our results against their fits (noting that there is a typo in their eq. 2.9; Z.-Y. Li, personal communication), where we present the radiation force multipliers as a function of the ionization parameter U (U is the ratio of hydrogen-ionizing photon density to hydrogen number density n, given by $U \equiv Q/4\pi n R^2 c$, where Q is the number of incident hydrogen-ionizing photons per second, and R is the distance from the continuum source). Overall, we find good agreement, especially considering that Arav et al. (1994) point out that their fit deviates from rigorous calculations at low values of U. The increase of our continuum force multiplier over theirs is most likely due to the different continuum opacity database included in Cloudy 96 Beta 4 compared to the code that was used in Arav et al. (1994). The multiplier values and trends with ionization parameter are still clearly very similar, however, which is encouraging.

We have also tested that the sputtering timescale of dust within the clouds and wind is less than the transit time of the gas through regions of high sputtering rate. To check this, we use the results of Tielens et al. (1994) to calculate the sputtering times (the times required to completely sputter away grains) throughout the wind and clouds. The transit timescale exceeds the sputtering timescale for the smallest ($a_{\min} = 50$ Å) grains for all of the models which include dust in the continuous wind; hence, sputtering is important for these grains. The clouds, on the other hand, have dust with sputtering timescales $\geq 10^7$ years. However, for the models with very low-density continuous wind ($n_0 = 10^6$ cm^{-3}), the sputtering timescale in the clouds can be as short as $\sim$ 3000 years, which is very close to the transit timescale of
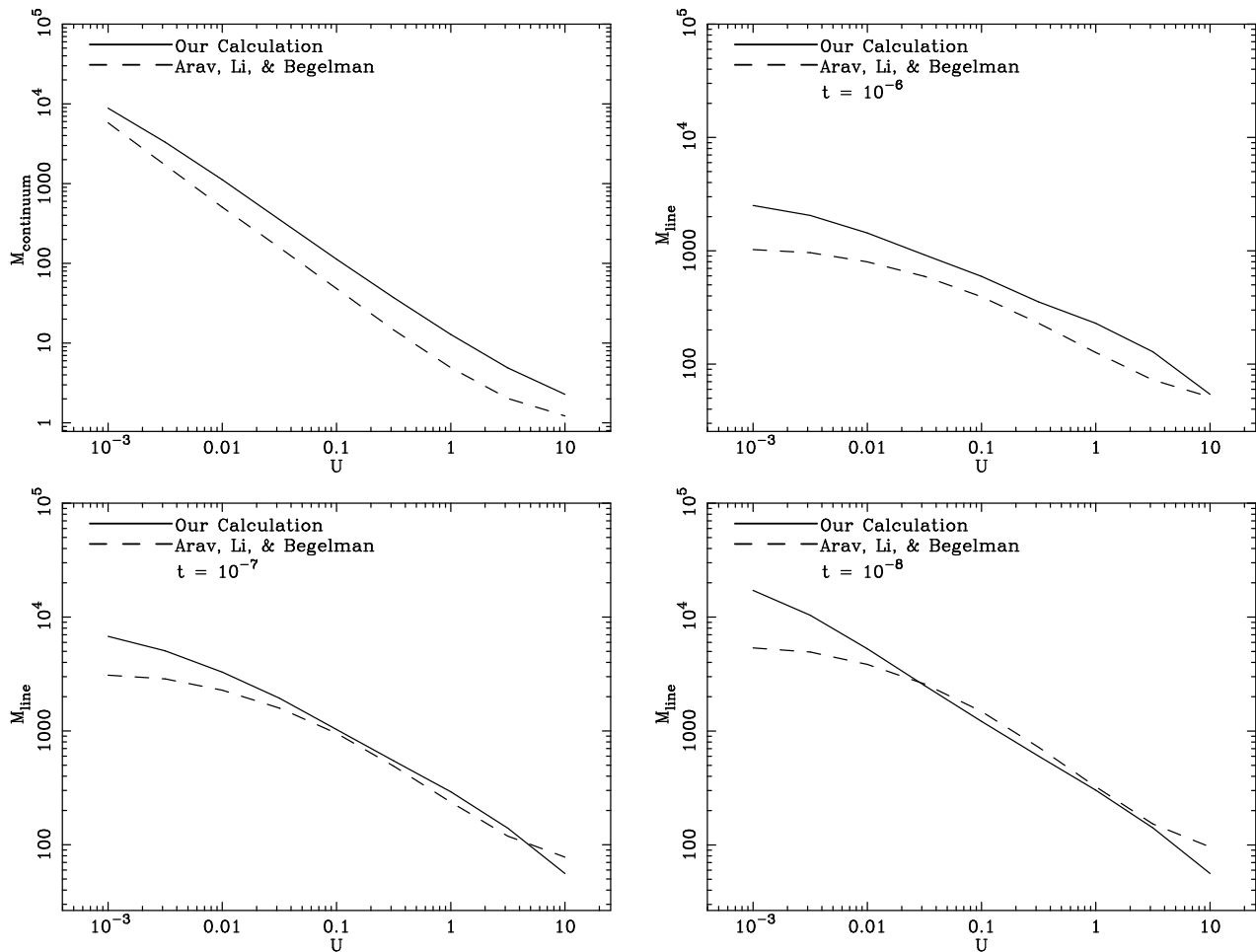
Fig. 2.— A comparison between the force multiplier calculation in our code (solid lines) and the fits of Arav et al. (1994) (dashed lines). The plot in the upper left is the comparison between our continuum force multiplier, as a function of the ionization parameter, U, and the earlier published fit. The next three panels show a comparison of the line force multiplier (which is also a function of t, besides U) as functions of U for three different values of t, given at the top of each panel. Overall, the agreement is fairly good, especially since the fits were known to deviate at low ionization parameter, U. The offset in the continuum multipliers is due to the different list of continuum opacities used, but the similar shape is encouraging.

~ 1000 years. For the time being, we do not change the dust distribution to take account of this sputtering; we simply note that a significant number of small grains may be sputtered in the wind (and perhaps some in the clouds). These calculations have, however, prompted us to examine solutions with an Orion dust distribution in the continuous wind: Orion dust does not have the smallest sized grains that are present in the ISM dust distribution. The comparison of Orion and ISM dust wind models will presented in Fig. 11.

3.4. *Integrating the Equation of Motion for the Wind*

Given the ionization and radiative acceleration information, our next step is to find the radiative acceleration of the continuous wind. We take the MHD wind model already computed and calculate the additional acceleration due to radiative forces. To do this, we derive the equation of motion for the wind, given by the Euler equation. We can then integrate that equation along the streamline of the MHD wind and record $\Gamma(\theta)$, the acceleration due to radiative forces.

In its simplest form, Euler's Equation is given as

$$\rho\left(\frac{\partial \mathbf{v}}{\partial t} + (\mathbf{v} \cdot \nabla)\mathbf{v}\right) = \sum \mathbf{F}_i, \tag{9}$$

where $\mathbf{F}_i$ represent all of the different forces in our system.

To specialize this equation for our wind, we first note that we are examining steady-state systems, so we neglect $\frac{\partial \mathbf{v}}{\partial t}$. As already mentioned, we neglect the thermal pressure but include gravitational, radiation, and Lorentz forces. In the expression below, we split the magnetic force term into pressure and tension components.

$$\rho(\mathbf{v} \cdot \nabla)\mathbf{v} = -[1 - \Gamma(\theta)]\frac{GM\rho}{R^2}\hat{R} - \frac{1}{8\pi}\nabla B^2 + \frac{1}{4\pi}(\mathbf{B} \cdot \nabla)\mathbf{B} \tag{10}$$

For our calculations, it will be more intuitive to integrate the equation of motion along the flow already given by the magnetocentrifugal wind solution. Thus, we take the dot product of Euler's equation with $\hat{s}$, which we define as the direction along the flow, expand, and simplify the left-hand side of the equation to read

$$((\mathbf{v} \cdot \nabla)\mathbf{v}) \cdot \hat{s} = v_p \frac{\partial v_p}{\partial s} - \frac{v_\phi^2}{r} \sin \theta_F, \tag{11}$$

where we define

$$\theta_F \equiv \tan^{-1}\left(\frac{dr}{dz}\right). \tag{12}$$

In the same way, if we define

$$\theta \equiv \tan^{-1}\left(\frac{r}{z}\right), \tag{13}$$

we can write out the gravitational term as

$$-[1 - \Gamma(\theta)]\frac{GM}{R^2}\hat{R} \cdot \hat{s} = -[1 - \Gamma(\theta)]\frac{GM}{(r^2+z^2)} \cos(\theta - \theta_F). \tag{14}$$

Next, we take the dot product of $\hat{s}$ with the magnetic terms to find

$$\left[-\frac{1}{8\pi\rho}\nabla B^2 + \frac{1}{4\pi\rho}(\mathbf{B} \cdot \nabla)\mathbf{B}\right] \cdot \hat{s} = -\frac{B_\phi}{4\pi\rho r}\frac{\partial(rB_\phi)}{\partial s}. \tag{15}$$

Bringing all of those terms back together into the Euler Equation, we can write

$$v_p \frac{\partial v_p}{\partial s} - \frac{v_\phi^2}{r} \sin\theta_F = -[1 - \Gamma(\theta)]\frac{GM}{(r^2 + z^2)} \cos(\theta - \theta_F) - \frac{B_\phi}{4\pi\rho r}\frac{\partial(rB_\phi)}{\partial s}. \tag{16}$$

We still have a v_ϕ dependence, however, that we can eliminate by appealing to the connection between v_p and v_ϕ in the Blandford & Payne model, which gives

$$v_\phi = \frac{v_p B_\phi}{B_p} + \Omega r. \tag{17}$$

We substitute this expression into our Euler Equation, which yields

$$v_p \frac{\partial v_p}{\partial s} - \left(\frac{v_p B_\phi}{B_p} + \Omega r\right)^2 \frac{\sin\theta_F}{r} = -[1 - \Gamma(\theta)]\frac{GM}{(r^2 + z^2)} \cos(\theta - \theta_F) - \frac{B_\phi}{4\pi\rho r}\frac{\partial(rB_\phi)}{\partial s}. \tag{18}$$

The only difficulty left is that, when we evaluate the radiative acceleration parameter t, we need to know $\frac{dv_R}{dR}$, the spherical, radial gradient of the spherical, radial velocity. Of course, we are integrating along the flow, and can only approximate the velocity gradients perpendicular to the flow. We approximate this gradient by calculating

$$\frac{dv_R}{dR} \approx \frac{dv_R}{ds}\frac{ds}{dR}, \tag{19}$$

$$\frac{dv_R}{dR} \approx \cos^2(\theta - \theta_F)\frac{dv_p}{ds}, \tag{20}$$

where the $\cos^2(\theta - \theta_F)$ term comes from approximating the geometry of our outflow.

3.4.1. Tests

We have tested the wind integration with radiative acceleration turned off, where it reproduces the original self-similar velocity profile to within one part in 10^5. With the radiative acceleration turned on, and without clouds present, the entire code has repeatedly converged within a few iterations to a "puffed out" magnetic wind structure, showing that radiation pressure does effect the wind. We have also tested this part of the code (again, without clouds) against Proga et al. (2000) and reproduced a similar final velocity, although we find somewhat higher velocities due to our inclusion of magnetic forces.

3.5. Euler Integrations for the Clouds

We are now in a position to calculate the motion of the clouds as they are pushed along by a mix of radiation pressure and the drag force felt through their relative motion with respect to the wind (the clouds are assumed to be diamagnetic, and thus are only confined by the magnetic field; they are not guided or accelerated by the magnetic fields in the continuous wind). The effect of the drag force is very important in two different ways. First, it is the primary source of cloud acceleration near the disk where the continuous wind launches the cloud by drag forces. In this case, the wind pulls the clouds along via drag, which slows the wind down. However, when the clouds feel significant radiative acceleration, the drag forces change sign, and the clouds help push the wind.

3.5.1. *Equation of Motion*

We integrate the following equations of motion for the clouds

$$\dot{v}_{r,cloud} = \frac{C_F \rho_{wind} R_{cloud}^2}{M_{cloud}} |\mathbf{v}_{wind} - \mathbf{v}_{cloud}|(v_{wind,r} - v_{cloud,r}) - [1 - \Gamma(\theta)]\frac{GM_\bullet}{r^2 + z^2} sin\,\theta \tag{21}$$

$$\dot{v}_{\phi,cloud} = \frac{C_F \rho_{wind} R_{cloud}^2}{M_{cloud}} |\mathbf{v}_{wind} - \mathbf{v}_{cloud}|(v_{wind,\phi} - v_{cloud,\phi}) \tag{22}$$

$$\dot{v}_{z,cloud} = \frac{C_F \rho_{wind} R_{cloud}^2}{M_{cloud}} |\mathbf{v}_{wind} - \mathbf{v}_{cloud}|(v_{wind,z} - v_{cloud,z}) - [1 - \Gamma(\theta)]\frac{GM_\bullet}{r^2 + z^2} cos\,\theta, \tag{23}$$

where R_{cloud} is the radius of the cloud, M_{cloud} is the mass of the cloud, and C_F is the constant drag coefficient (for the solutions presented here, we use $C_F = 10$, Blandford & Königl 1979), and the overdot indicates derivatives with respect to time. The only non-trivial calculation is again the determination of the radiative acceleration.

3.5.2. *Radiative Acceleration*

For the calculation of radiative acceleration on the clouds, we can use the same equations that we used for the continuous wind, with two exceptions: the definition of t and the equation for $\frac{dv_R}{dR}$.

To calculate the effective electron optical depth (t) for the clouds, we must take into account that the clouds do not fill all of the wind. We therefore define:

$$t_{cloud} \equiv \frac{\sigma_T \epsilon n_e v_{th}}{\frac{dv_R}{dR}}, \tag{24}$$

where ϵ is the fraction of the wind volume taken up by the clouds (see Arav et al. 1994). This factor is very important as the matter in the clouds only occupies a small fraction of the wind volume, and so the opacity is much smaller than it would be for the continuous wind, for instance.

Once again, we must calculate $\frac{dv_R}{dR}$, where R is the spherical radial coordinate. We can go through a more rigorous calculation than before by first recognizing that, since we are following the clouds as a function of time, the total derivative is

$$\frac{dv_R}{dR} = \frac{\partial v_R}{\partial t}\frac{\partial t}{\partial R} + \frac{\partial v_R}{\partial r_0}\frac{\partial r_0}{\partial R}, \tag{25}$$

where r_0 is the cylindrical radius of the footpoint where the cloud started to rise from the disk. Since $v_R = v_p \cos(\theta - \theta_F)$, we write

$$\frac{\partial v_R}{\partial t} = \frac{1}{v_p}\left(v_r\frac{dv_r}{dt} + v_z\frac{dv_z}{dt}\right)\cos(\theta - \theta_F) +$$
$$-v_p\sin(\theta - \theta_F)\left(\frac{d\theta}{dt} - \frac{d\theta_F}{dt}\right). \tag{26}$$

The derivatives of angles θ and θ_F are self-consistently computed from their definitions

$$\theta = \tan^{-1}\left(\frac{r}{z}\right) \tag{27}$$

$$\Rightarrow \frac{d\theta}{dt} = \frac{1}{1 + (r/z)^2}\left(\frac{1}{z}\frac{dr}{dt} - \frac{r}{z^2}\frac{dz}{dt}\right) = \frac{1}{1 + (r/z)^2}\left(\frac{1}{z}v_r - \frac{r}{z^2}v_z\right), \tag{28}$$

and

$$\theta_F = \tan^{-1}\left(\frac{v_r}{v_z}\right) \tag{29}$$

$$\Rightarrow \frac{d\theta_F}{dt} = \frac{1}{1 + (v_r/v_z)^2}\left(\frac{1}{v_z}\frac{dv_r}{dt} - \frac{v_r}{v_z^2}\frac{dv_z}{dt}\right). \tag{30}$$

Meanwhile, for the other terms in the equation, we write

$$\frac{\partial t}{\partial R} = \frac{1}{v_R} \tag{31}$$

$$\frac{\partial v_R}{\partial r_0} = -\frac{v_R}{2r_0}, \tag{32}$$

where, for the last equation, we assume that the gradient of the velocity with respect to the starting radius scales according to the Keplerian relation.

Finally, to calculate the derivative $\frac{\partial r_0}{\partial R}$, we assume that the flowlines do not change direction rapidly along the spherical, radial line of sight. Then, from trigonometry, we find

$$\frac{\partial r_0}{\partial R} = \sin\theta - \cos\theta\tan\theta_F \tag{33}$$

Bringing all of those terms together, and simplifying, we have the following expression:

$$\frac{dv_R}{dR} = \frac{v_r\dot{v}_r + v_z\dot{v}_z}{v_p^2} - \frac{\sin(\theta - \theta_F)}{\cos(\theta - \theta_F)}\left(\dot{\theta} - \dot{\theta}_F\right) - \frac{v_p\cos(\theta - \theta_F)}{2r_0}\left(\sin\theta - \cos\theta\tan\theta_F\right). \tag{34}$$

3.5.3. *Calculating Drag Forces on the Wind*

We next integrate the cloud equations of motion, recording the position and velocity of the clouds as a function of angle above the disk. We also output the radiative force on the clouds and, in order to calculate the drag on the continuous wind, the drag forces of the clouds on the wind. We calculate those drag forces almost exactly the same way we computed the drag force of the wind on the clouds, except that now we must include the effect of many clouds on the wind, taking into account the ensemble density of clouds.

The radial component of the wind's drag force on the clouds is given by the following force equation (for simplicity, we follow just the radial equation, here; the other components [azimuthal and vertical] are very similar except for the final term which is the difference of that component's velocities):

$$F_{r,drag,cloud} = C_F \rho_{wind} R_{cloud}^2 |\mathbf{v}_{wind} - \mathbf{v}_{cloud}|(v_{wind,r} - v_{cloud,r}). \tag{35}$$

The force of any given cloud back on the wind is equal and opposite to this,

$$F_{r,drag,wind} = -C_F \rho_{wind} R_{cloud}^2 |\mathbf{v}_{wind} - \mathbf{v}_{cloud}|(v_{wind,r} - v_{cloud,r}). \tag{36}$$

To find the acceleration from this drag force, which we use as an additional acceleration in our self-similar continuous wind model, we then write

$$\rho_{wind} V_{wind\ per\ cloud} a_{r,wind} = -C_F \rho_{wind} R_{cloud}^2 |\mathbf{v}_{wind} - \mathbf{v}_{cloud}|(v_{wind,r} - v_{cloud,r}), \tag{37}$$

where $V_{wind\ per\ cloud}$ is the wind volume per cloud, $V_{wind\ per\ cloud} = n_{cloud,ens}^{-1}$. Substituting this in yields:

$$\rho_{wind} n_{cloud,ens}^{-1} a_{r,wind} = -C_F \rho_{wind} R_{cloud}^2 |\mathbf{v}_{wind} - \mathbf{v}_{cloud}|(v_{wind,r} - v_{cloud,r}). \tag{38}$$

After some simplification,

$$a_{r,wind} = -C_F n_{cloud,ens} R_{cloud}^2 |\mathbf{v}_{wind} - \mathbf{v}_{cloud}|(v_{wind,r} - v_{cloud,r}) \tag{39}$$

For interface into the self-similar wind models, we just divide by the gravitational acceleration, so this force can be included in the same way that $\Gamma(\theta)$ is included in the self-similar model. Therefore, we define

$$\Delta_r = \frac{-C_F n_{cloud,ens} R_{cloud}^2 |\mathbf{v}_{wind} - \mathbf{v}_{cloud}|(v_{wind,r} - v_{cloud,r})}{GM_\bullet/(r^2 + z^2)}, \tag{40}$$

where the other components of the drag equation would yield similar expressions for Δ_ϕ and Δ_z, the drag in the azimuthal and vertical directions.

The function $\Delta_r(\theta)$ is input back into both the self-similar MHD wind solver as well as the program that computes the continuous wind's radiative acceleration. In the case of the self-similar wind, we must be careful to only include the spherical radial component of the drag force, in order to not disturb the self-similar nature of those equations (since we are including this force as a modification to gravity, it must also scale as gravity, depending only on the spherical radius R). Thus, the quantity input back into the self-similar wind model is:

$$\Delta_R = \Delta_r \sin\theta + \Delta_z \cos\theta. \tag{41}$$

In the program that integrates Euler's equation to find the continuous wind's radiative acceleration, we also include the drag force, but in a slightly different way. Since that program computes the poloidal velocity of the wind, v_p, it uses only the poloidal component of the drag force in modifying its force laws. Within that program, we therefore calculate

$$\Delta_P = \Delta_r \sin\theta_F + \Delta_z \cos\theta_F. \tag{42}$$

These accelerations are included in successive iterations of the code.

4. EARLY RESULTS

In this section, we outline further tests of our model, and end by using the model to explore the dependence of the wind on key input parameters.

4.1. *Tests of Code Convergence*

We first show that with this model setup, the iterations in the model converge to a stable solution, after which successive iterations of the code do not significantly alter the structure of the wind (see Fig. 3). Almost as important, the system converges to a solution within just a few iterations, corresponding to approximately a day of computational time on a standard desktop workstation.

4.2. *Testing Other Radiative Acceleration Approximations*

Our early runs with this model have given interesting results when comparing this work to previous research on AGN outflows. One of our first checks on the radiative acceleration code was to compare with previous published results to see if we obtain similar acceleration factors. We found that, considering the continuous wind's radiative acceleration alone and assuming an MF87 input spectrum, the wind experienced much less acceleration than with the continuum from MCGV95 (see Fig. 4). This agrees well with the results of MCGV95, and shows the sensitivity of radiative acceleration not only to the incident spectrum, but also to the shielding that lies between the outflowing wind and the central source, which has a strong impact on the spectrum incident on the outflowing gas.
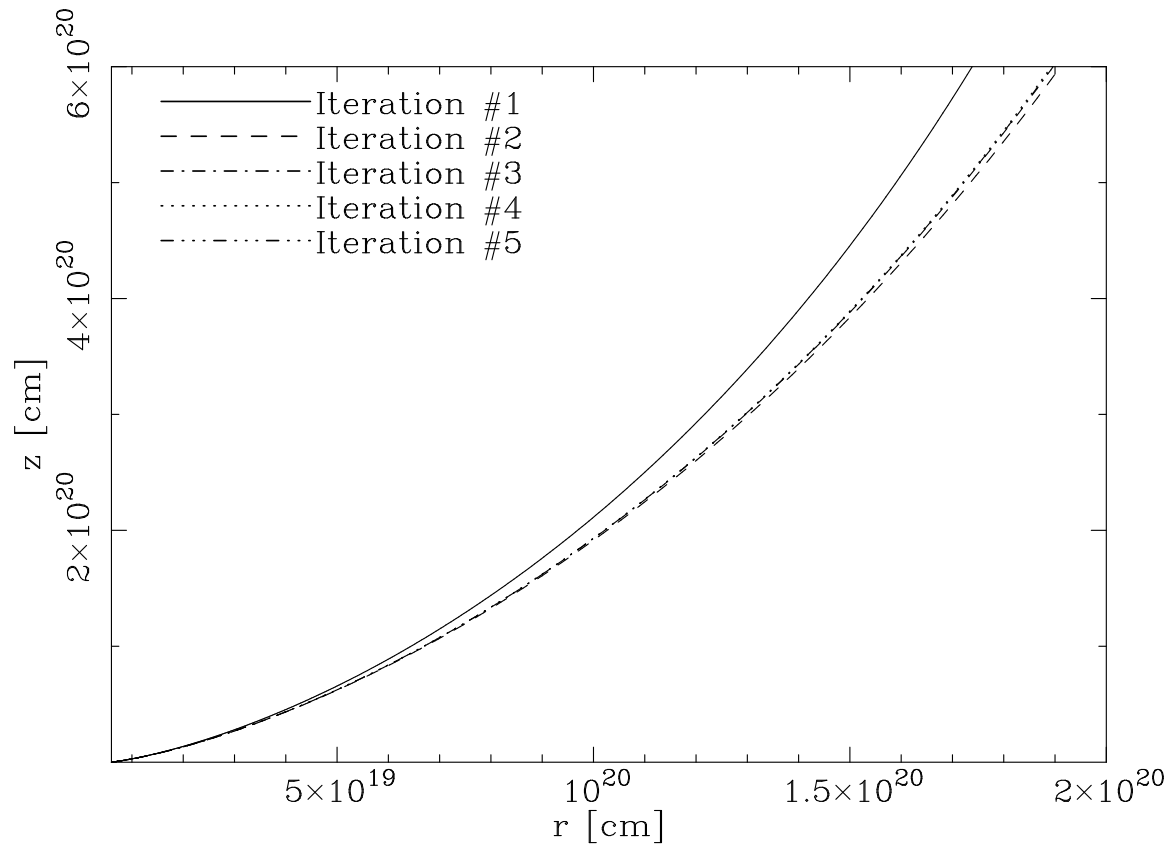
Fig. 3.— A plot of the poloidal wind streamlines in our model and their evolution over several iterations of the code. After the third iteration, the solution does not change, and the lines overlap, indicating convergence for this outflow.
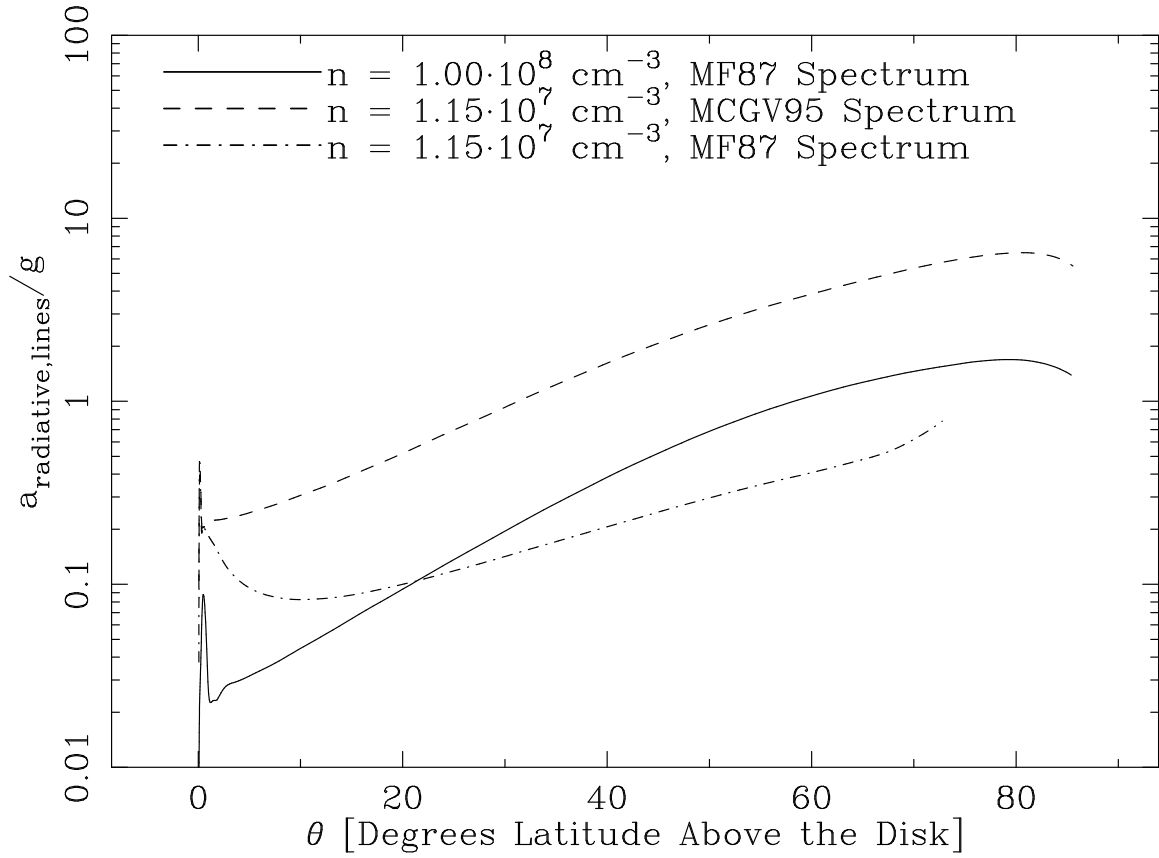
FIG. 4.— A comparison of the radiative acceleration obtained with different incident spectrum, showing the MF87 spectrum and the spectrum assumed in MCGV95. For the initial wind density of 10^7 cm^{-3}, the MCGV95 spectrum yields much greater acceleration than the Mathews & Ferland spectrum. Note that this solution does not include clouds, allowing a better comparison with the continuous wind simulations of MCGV95.
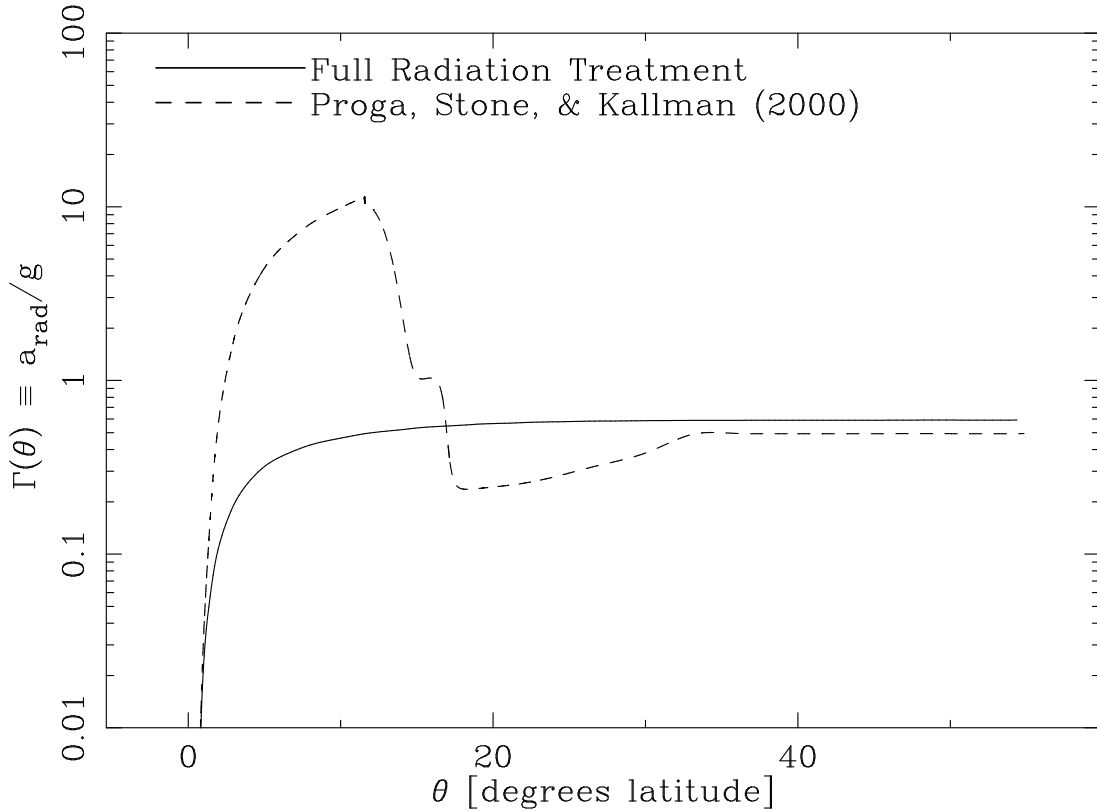
FIG. 5.— A comparison between our full radiation treatment and calculations equivalent to those used given in Proga et al. (2000).

In another comparison with previous research, we re-programmed the model to calculate radiative acceleration using the same approximations as were used in Proga et al. (2000). We were also careful to use the same incident 10 keV bremsstrahlung spectrum that was assumed in their work when they employed the results of Stevens & Kallman (1990). When we inserted that radiation handling into our model, we found very different radiative acceleration profiles than shown in our calculations using Cloudy photoionization results. This difference could be due to a couple of factors. First, in Proga et al. (2000), it is also assumed that the fraction of flux in the X-ray and UV portions of the spectrum were equal (both set to half of the incident flux). As was shown later (Proga et al. 2002), the balance of X-ray and UV radiation in the incident spectrum is critically important: while the UV radiation is the primary source of momentum for the gas, the X-ray radiation ionizes the gas, and the more X-ray radiation present in the spectrum, the fewer lines remain in the gas to absorb the momentum from UV photons. If the 10 keV bremsstrahlung spectrum does not have this balance of UV and X-ray flux, it could be a source of error in the calculations. Second, the 2D hydro simulations only use estimates of the ionization parameter rather than calculate it exactly.

We must point out here that our goal is to test different methods of computing radiative acceleration and check whether approximations give the same result as our *ab initio* calculations. From this study, within the framework and assumptions of our model, we can only conclude that the approximations used in Proga et al. (2000) do not match the radiative acceleration calculated from first principles. However, it is also important to realize that such approximations allow those researchers the ability to simulate larger-scale flows, which can lead to valuable insight. We believe, though, that these figures show the necessity of accurately handling the radiation transfer and acceleration calculations.

In the subsection that follows, we perform a parameter survey, noting the cases where radiative acceleration significantly affects the geometry and kinematics of our wind models.

TABLE 1
FIDUCIAL PARAMETERS ADOPTED FOR THE MODELS IN THIS PAPER.[a]

Parameter	Fiducial Value	Parameter Description
κ	0.03	dimensionless ratio of mass flux to magnetic flux in the wind
λ	30.0	normalized total specific angular momentum of the wind
b	1.5	power-law describing variation of density with spherical radius at the base of the wind: $n \propto R^{-b}$
$M_\bullet$	$10^8 M_\odot$	mass of the central black hole
$L_{\rm continuum}$	$0.25\ L_{\rm Edd}$	luminosity of the central continuum
Incident Spectrum	Mathews & Ferland (1987)	Spectrum for the central continuum
r_0	6×10^{18} cm	launch radius of the continuous wind
n_0	10^8 cm^{-3}	initial density of the continuous wind at the launch radius
$N_{\rm H,shield}$	10^{25} cm^{-2}	gas shielding column at the base of the wind
Dust in Continuous Wind	No	presence of dust in the continuous wind
$M_{\rm cloud}$	$10^{-2} M_{\rm cloud,max}$	mass of the cloud as a fraction of the maximum cloud mass the wind can uplift by ram pressure
$\dot{M}_{\rm cloud}$	$10^{-2} \dot{M}_{\rm wind}$	mass outflow rate of the clouds as a fraction of the mass outflow rate of the wind
C_F	10	dimensionless geometrical drag coefficient of the clouds

[a]Any changes to these parameters are listed in the figure captions.

TABLE 2
RANGE OF VALUES EXAMINED IN THE PARAMETER SURVEY AND RELEVANT FIGURES FOR EACH PARAMETER

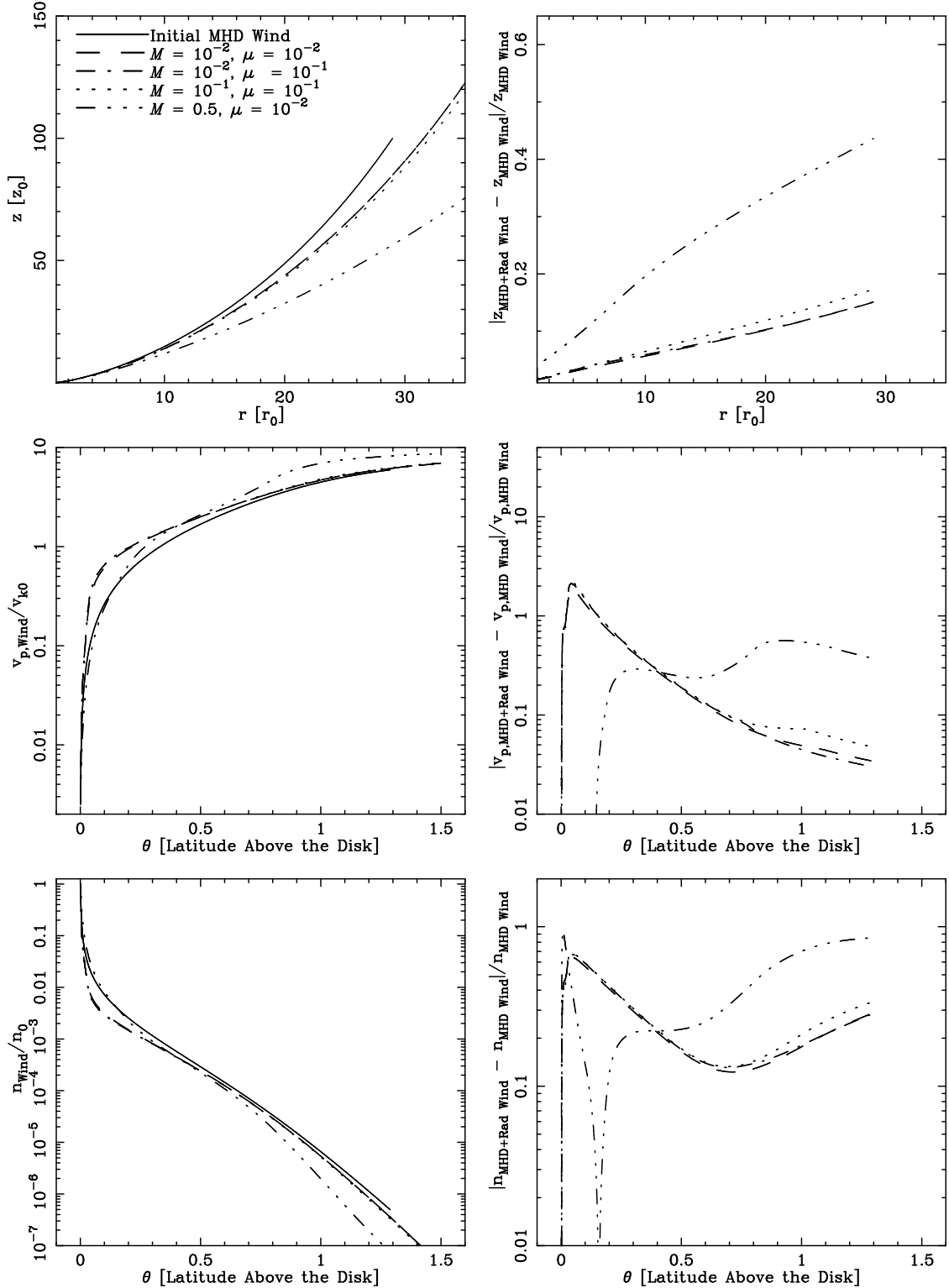| Parameter	Range of Values	Figure(s)
$M_{\rm cloud}$	$0.01 - 0.1 M_{\rm cloud,max}$	6
$\dot{M}_{\rm cloud}$	$0.01 - 0.5 \dot{M}_{\rm wind}$	6
r_0	$6 \times 10^{17} - 6 \times 10^{19}$ cm	7, 13
n_0	$10^6 - 10^{10}$ cm^{-3}	8
$N_{\rm H,shield}$	$10^{22} - 10^{26}$ cm^{-2}	9, 10
Dust in Continuous Wind	No Dust, ISM Dust, Orion Dust	11
$L_{\rm continuum}$	$0.1 - 0.5\ L_{\rm Edd}$	12, 15
Incident Spectrum	MF87, MCGV95	12, 15
κ	$0.015 - 0.1$	14, 16
$M_\bullet$	$10^7 - 10^9 M_\odot$	17

FIG. 6.— The six panels of this figure display the variation in the wind model with changes in the cloud parameters: we vary both the mass outflow rate of the clouds and the mass of the individual clouds. The plots on the left give the poloidal streamlines of the wind, the poloidal velocity, and the density of the wind. For each of these figures, the solid black line gives the initial MHD wind model (without radiative acceleration) and the various broken lines give the wind's equilibrium structure after radiative acceleration has been applied. In the three plots on the right, that equilibrium structure is compared to the initial MHD wind structure by plotting the difference between the initial and final wind model divided by the initial MHD wind results. For this plot, we define $M = \dot{M}_{\rm cloud}/\dot{M}_{\rm wind}$ and the cloud mass $\mu = M_{\rm cloud}/M_{\rm cloud,max}$. The low initial velocity difference and large drop in the variation of wind density in the high cloud outflow case is due to the large drag exerted by the clouds on the wind when the wind launches the clouds from the disk.
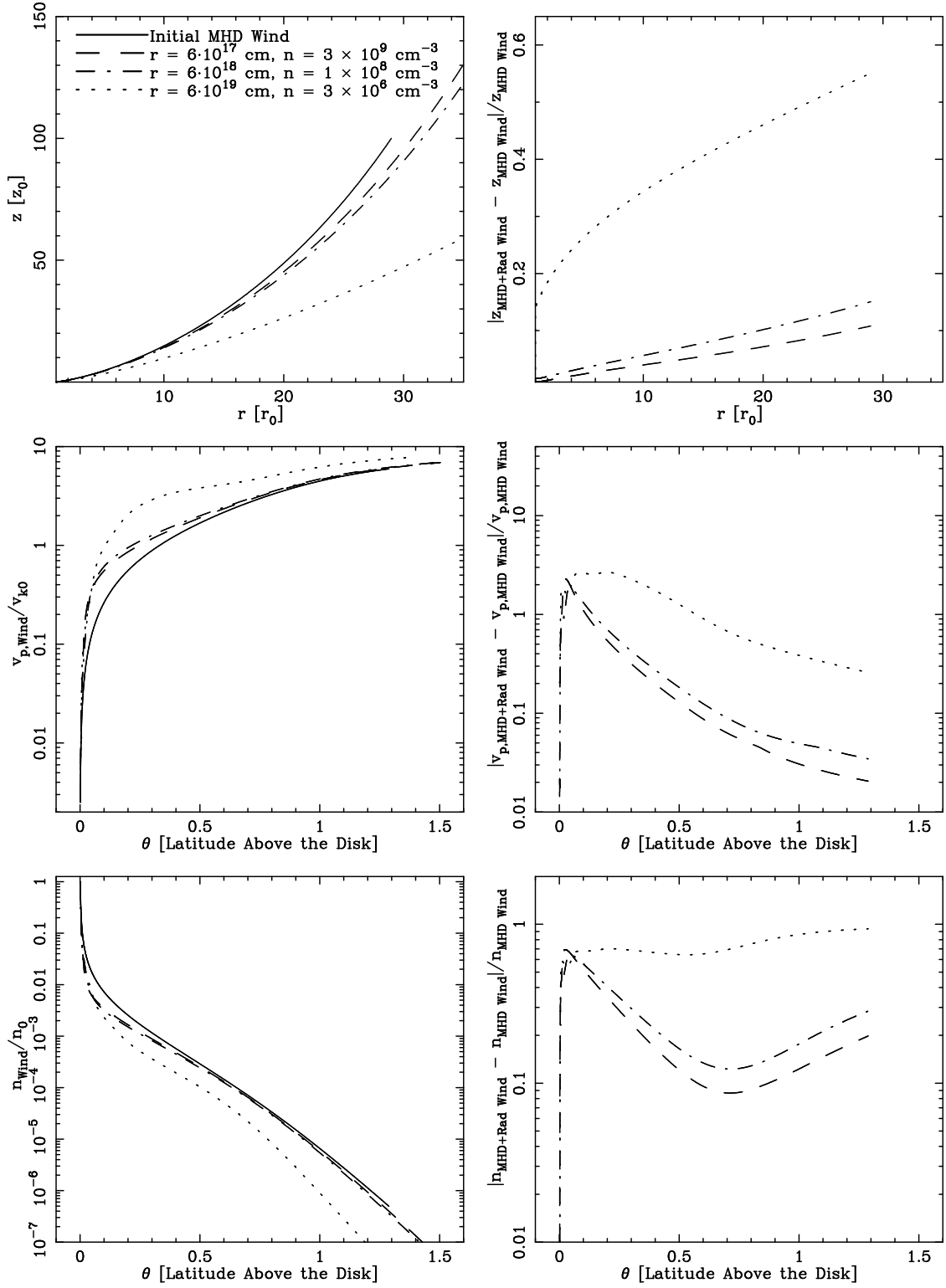
FIG. 7.— As in Fig. 6, but showing the variation in wind structure with changes in the launching radius of the continuous wind.
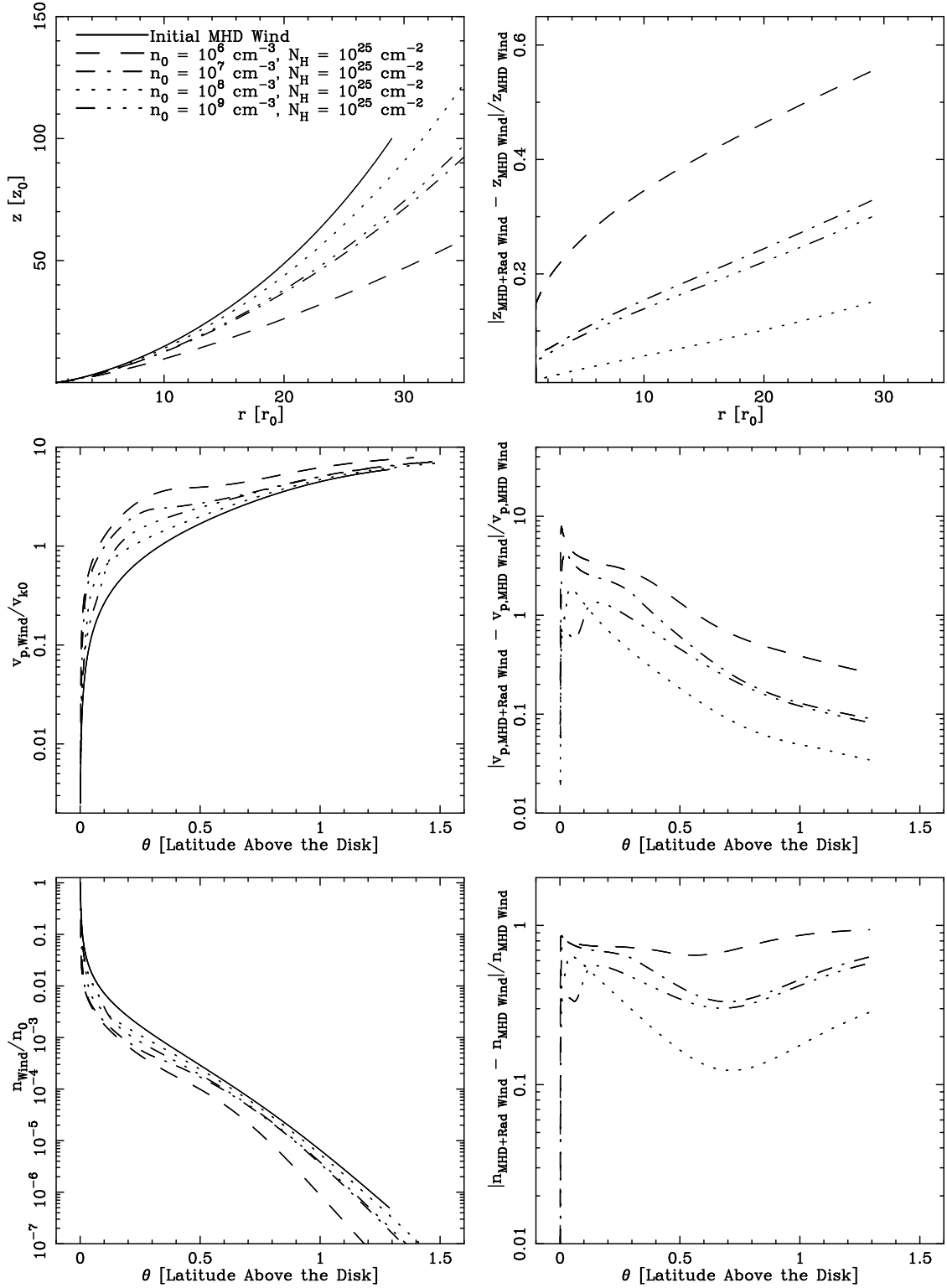
Fig. 8.— As in Fig. 6, but showing the variation in wind structure with changes in the initial density of the continuous wind.
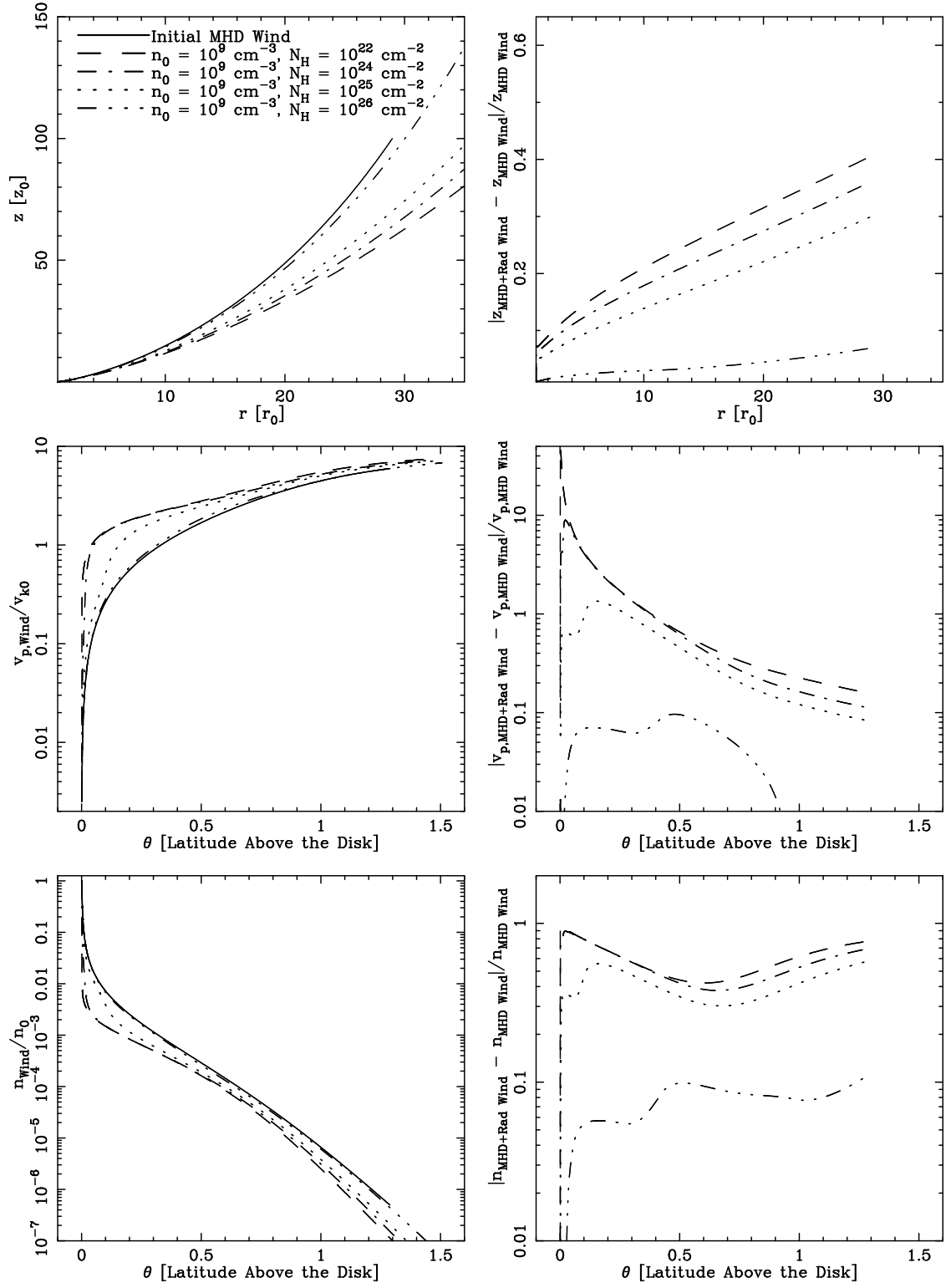
FIG. 9.— As in Fig. 6, but showing the variation in the wind structure with changes in the shielding gas column in front of the wind, and with an initial wind density of 10^9 cm^{-3}.
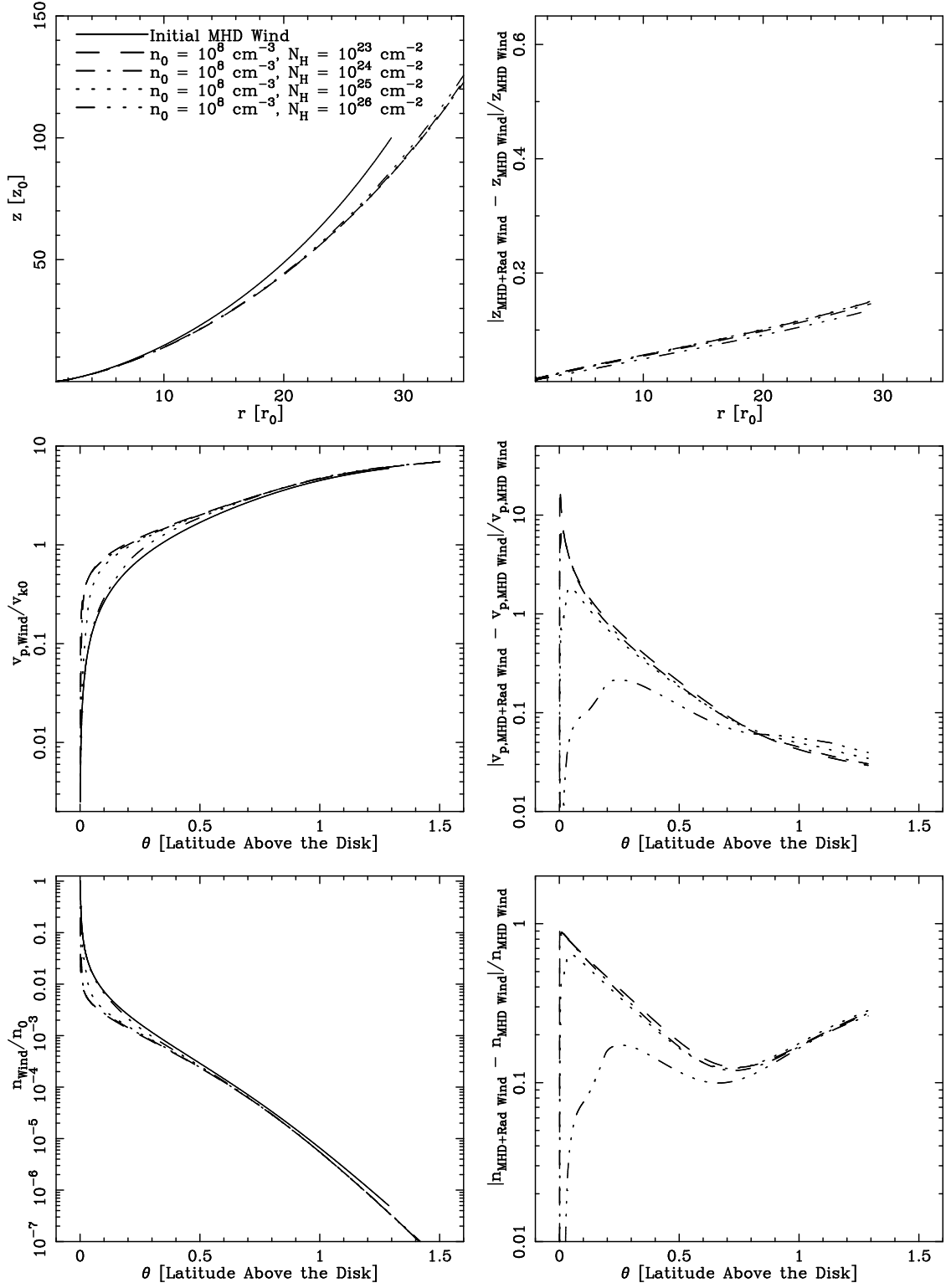
FIG. 10.— As in Fig. 6, but showing different levels of gas shielding in front of the outflow for an initial wind density of 10^8 cm^{-3}.
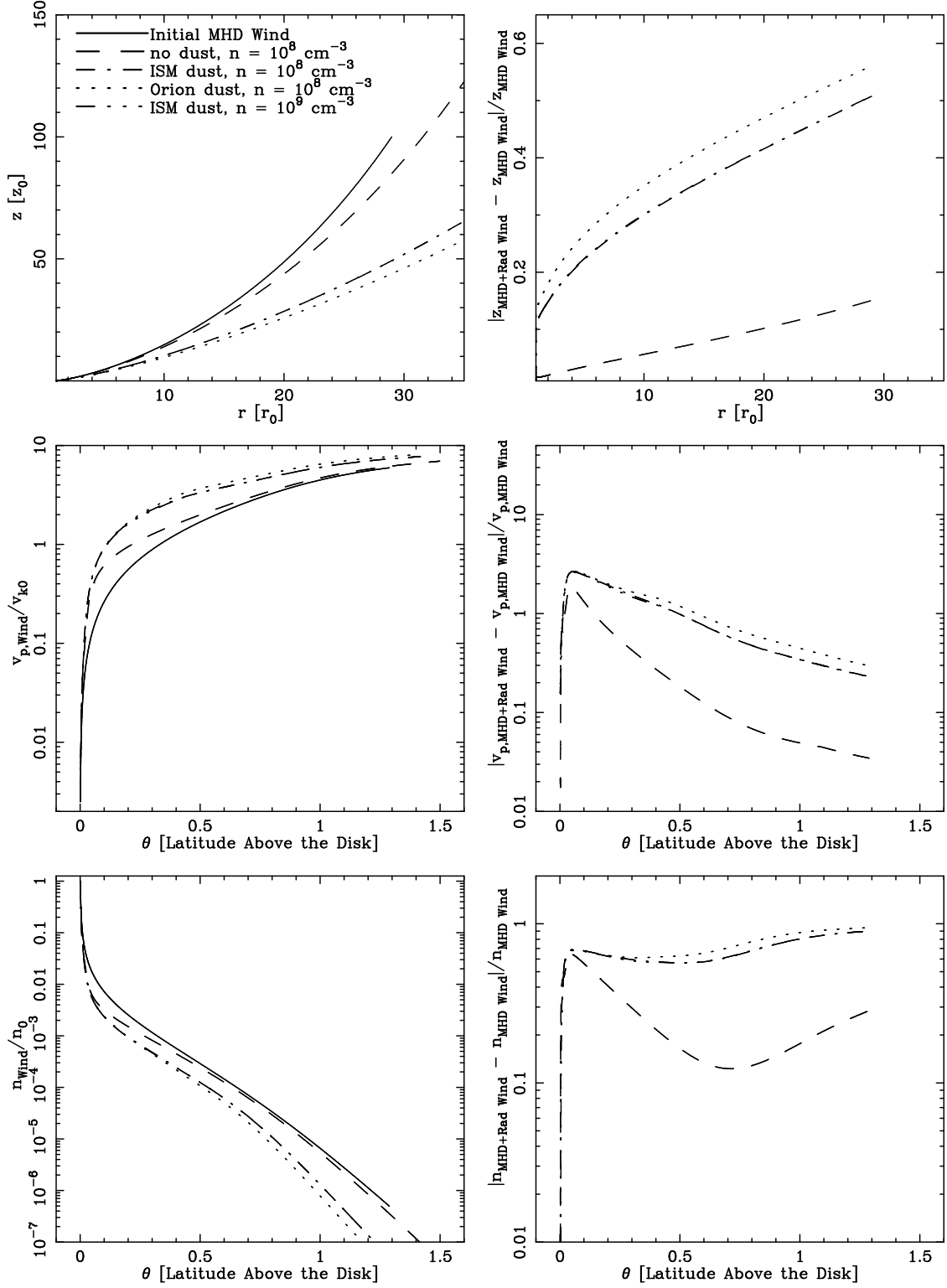
FIG. 11.— As in Fig. 6, but showing the variation in wind structure when dust is included in the continuous wind.
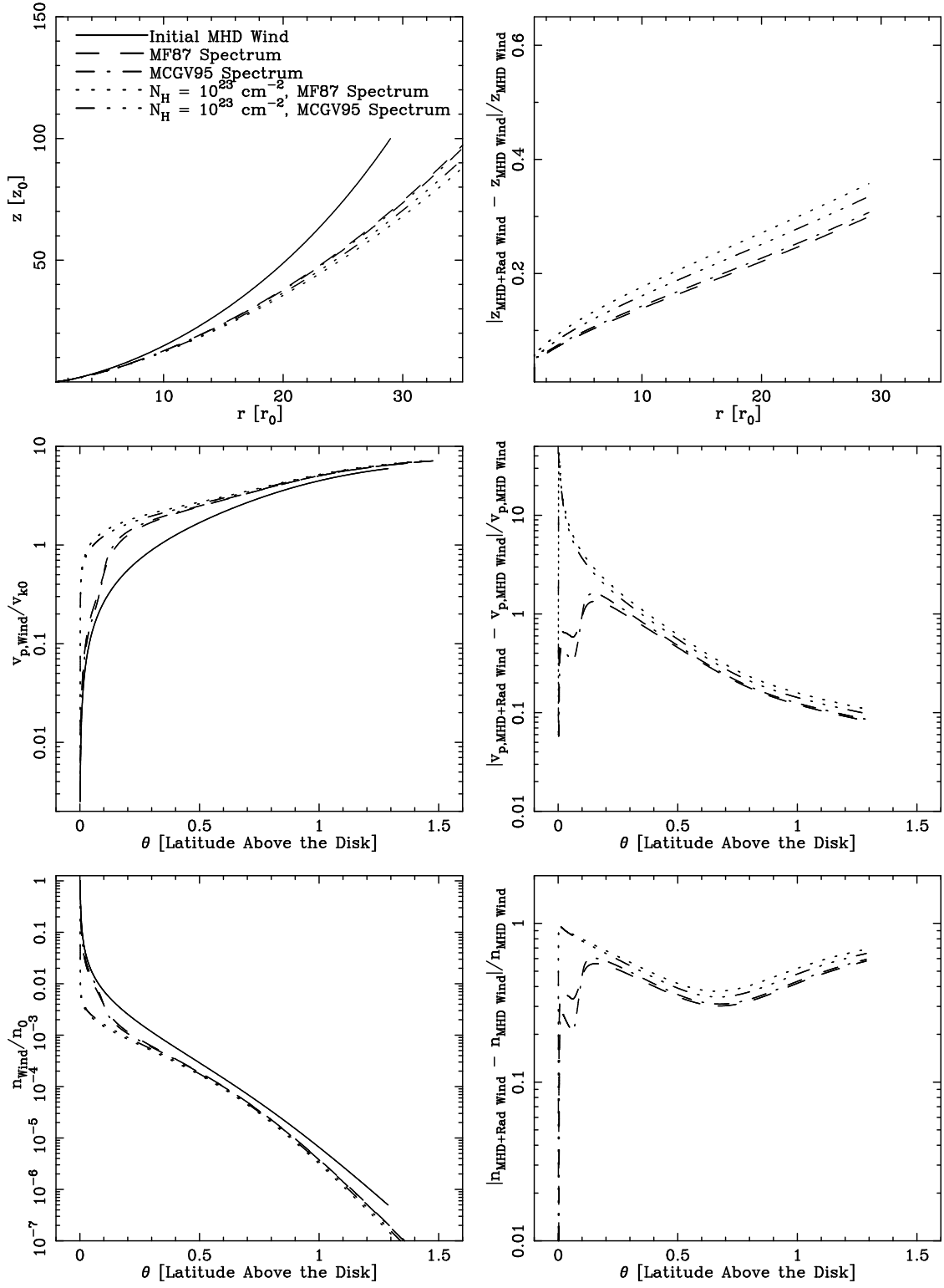
Fig. 12.— As in Fig. 6, but showing the variation in the wind structure with changes in the incident continuum and shielding. All of the solutions here were run with an initial wind density of $n_0 = 10^9$ cm^{-3}
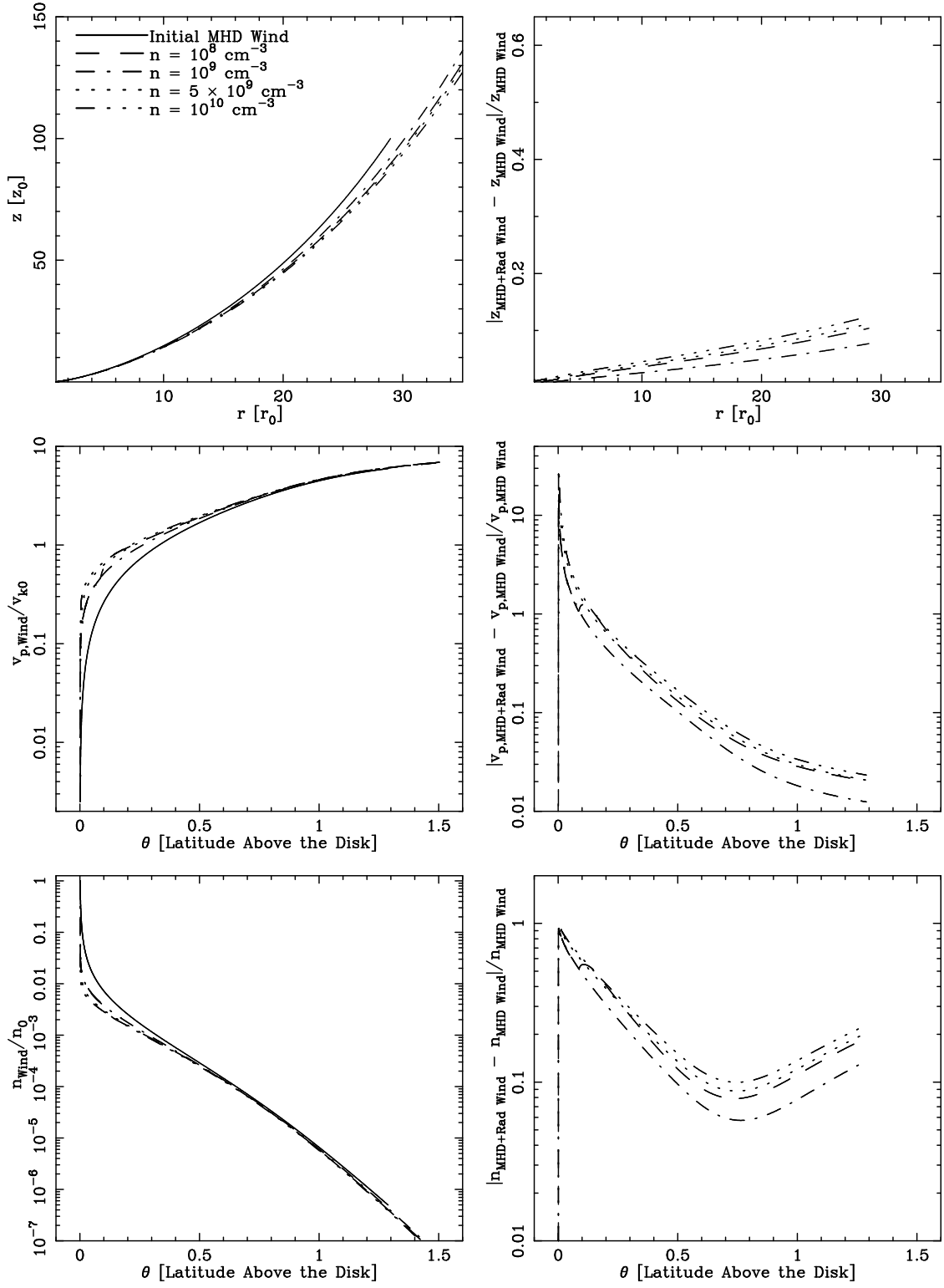
FIG. 13.— As in Fig. 6, but showing the variation in wind structure when the wind is launched at a radius an order of magnitude closer to the central black hole. All of the runs shown here have an initial launch radius $r_0 = 6 \times 10^{17}$ cm and shielding columns of $N_H = 10^{23}$ cm^{-3}.
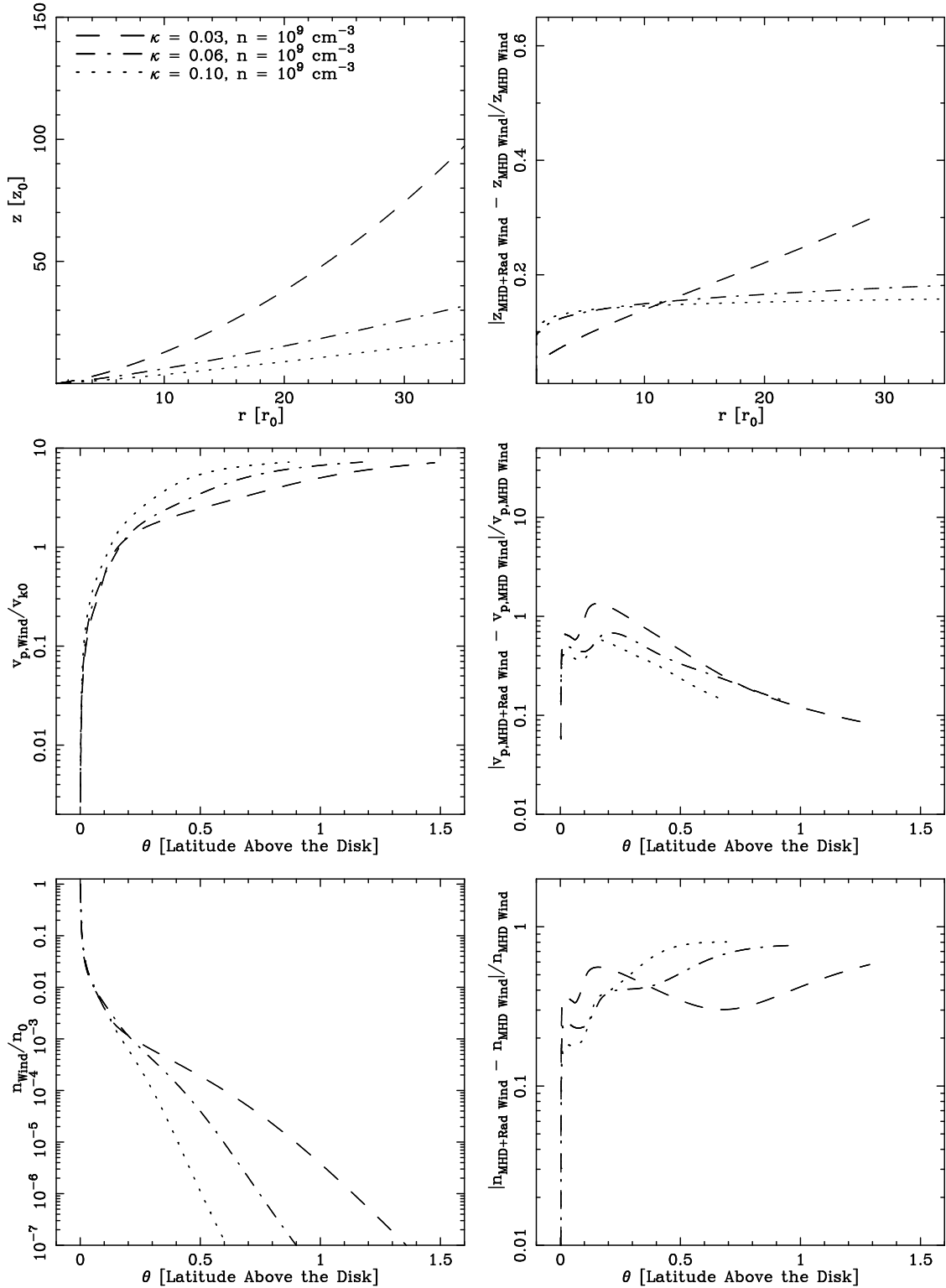
FIG. 14.— As in Fig. 6, but showing the variation in wind structure with changes in κ (the dimensionless mass to magnetic flux ratio in the wind) for wind models with an initial wind density of 10^9 cm^{-3}. These plots differ from the other parameter-variation plots given: as κ is changed, the basic MHD wind model changes, so each model shown has its own pre-radiative acceleration MHD wind model. To avoid confusion, therefore, none are shown on the left panels, and each of the different plots on the right compare the initial MHD wind model *for that value of* κ and the final equilibrium model. Also, note that the end-points of the models (in altitude) are not the same for all models; this is because the models are plotted as a function of θ, and even though the models all end at the same absolute height, θ is smaller because the wind is less collimated and hence farther from the central source, ending at a smaller value of θ.
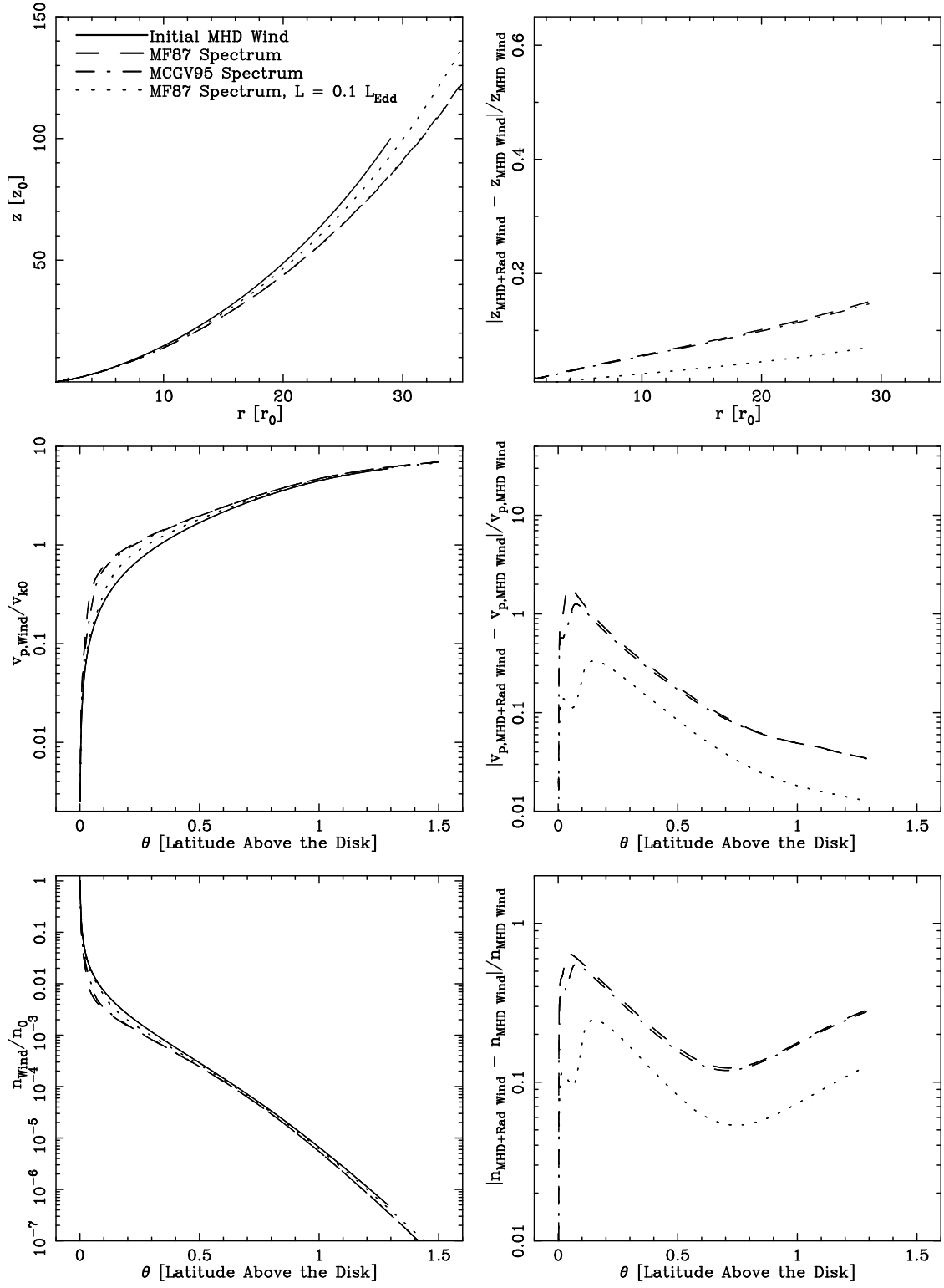
Fig. 15.— As in Fig. 6, but showing the variation in the wind structure with changes in the incident continuum. All of the solutions here have an initial wind density of $n_0 = 10^8$ cm^{-3}
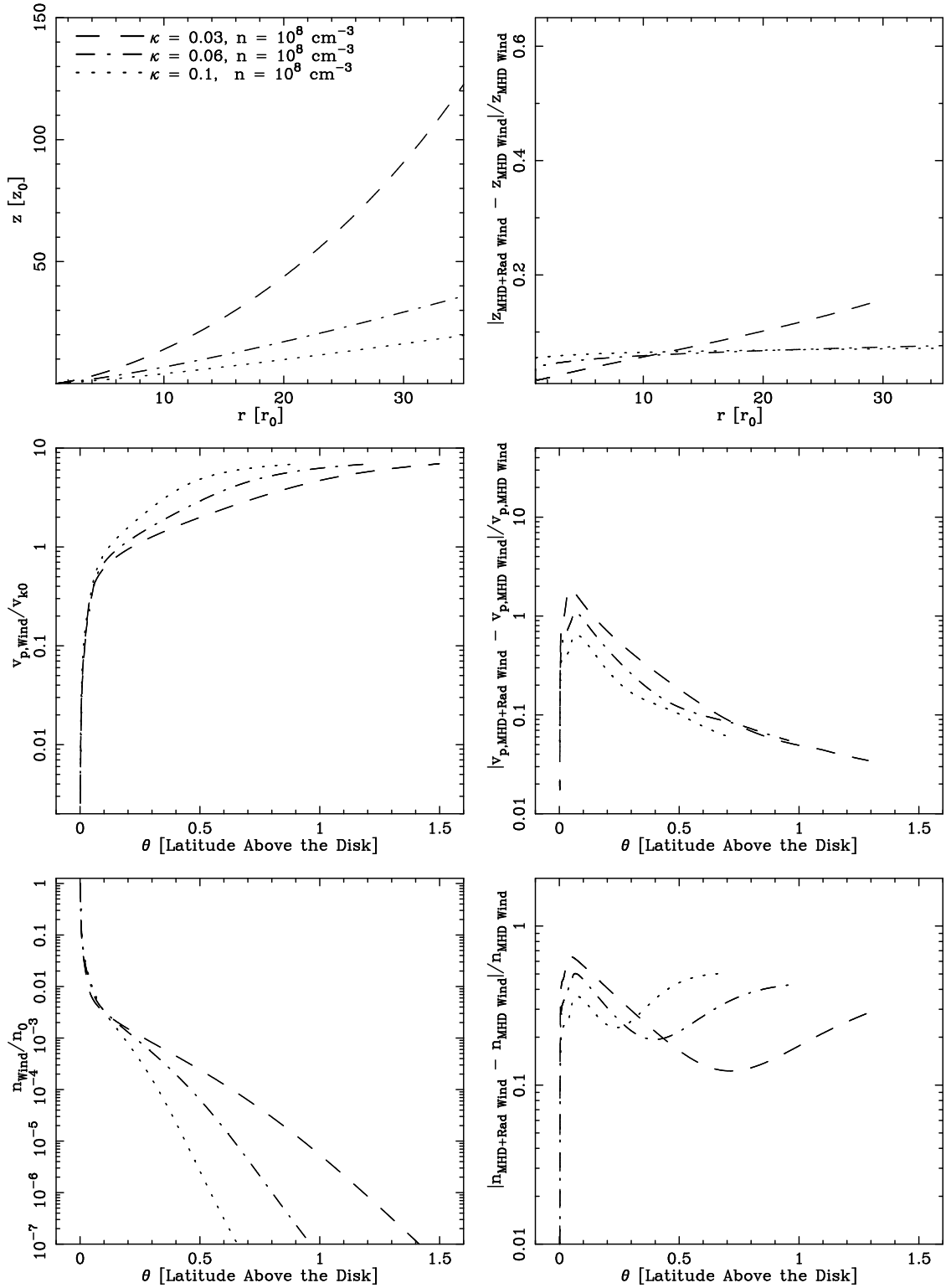
FIG. 16.— As in Fig. 14, but showing the variation in wind structure with changes in κ (the dimensionless mass to magnetic flux ratio in the wind) for wind models with an initial wind density of 10^8 cm^{-3}.

4.3. *Parameter Survey*

4.3.1. *Setup*

In this parameter survey, we compare the variations in the wind's velocity, density, and radiative acceleration when we change key parameters in the wind model. Unless otherwise indicated, parameters retain fiducial values adopted for the purpose of this paper (see Table 1). A summary of the variations that we have explored is shown in Table 2.

4.3.2. *Results*

Key results from our parameter survey are shown in Figures 6 to 17, which are described in detail below.

A very interesting result from this survey is how important embedded clouds are in driving the wind to new geometries and higher velocities. The most dramatic example of the interaction of clouds is shown in Figure 6, where we vary both the mass of the clouds and the mass outflow rate of cloud material. In this figure, for high cloud mass-outflow rates, we find large changes in wind structure and kinematics.

The great importance of clouds stems from four major differences between the clouds and the wind: the low volume filling factor of the clouds, the lower ionization of the cloud material due to high density relative to the continuous wind, dust within the clouds, and the fact that our clouds are not magnetically driven – they are free to follow purely radial trajectories through the centrifugally driven wind. The low filling factor decreases the opacity of cloud material, thereby decreasing $t_{\rm cloud}$ (see the definition of $t_{\rm cloud}$ in eq. [24]). This low filling factor then leads to an increase in the line force multiplier (see eq. [7] and Fig. 2, which shows the increase in force multiplier with decrease in t) and accelerates the clouds much more than the surrounding, continuous wind, where the line opacity is much higher. The clouds can then drag the wind with them and significantly alter the wind when the mass outflow fraction of the clouds is high enough. As is shown in Figure 6, for $\dot{M}_{\rm cloud} = 0.5~\dot{M}_{\rm wind}$, the clouds have a very large impact on the continuous wind's geometry and velocity. This is due largely to the large mass outflow rate in the clouds, but also to the lower opacity of the cloud material, as well as the lower ionization parameters that exist in the more dense clouds. The lower ionization parameters in the clouds mean that the gas is less ionized, yielding more possible continuum transitions, and resulting in a higher continuum force multiplier (the increase of the continuum force multiplier with the ionization parameter, U, is also shown in Figure 2).

Dust can also be an important source of opacity and hence radiative driving for clouds, although for many of the outflows within our survey, dust cannot survive because its temperature in the clouds quickly rises above the sublimation temperature. In general, in survey, dust only survives in the clouds when there is very significant shielding of a high-density wind ($N_H \geq 10^{26}{\rm cm}^{-2}$), a comparatively low central luminosity (of order $0.1L_{\rm Edd}$), or if the clouds are contained and shielded in a dusty wind. In each of these cases, the resultant low luminosity striking the clouds means that even though dust is present, very little radiative acceleration results from it. However, if we move the wind out to larger radii, as shown in Figure 7, dust is able to survive in the clouds and asserts critical importance in modifying the wind structure: in the case of the $r = 6 \times 10^{19}$ cm solution, the radiative acceleration due to the continuum in the clouds overwhelms line driving in the clouds by a factor of ~ 100. This is also the reason behind the increase in velocity for the $n_0 = 10^6$ cm^{-3} model in Figure 8, where we show the effect of modifying the wind's initial density. Dust can also survive within the clouds in this model, yielding higher continuum radiative acceleration, and pushing the wind to higher velocities than otherwise possible. Without dust, the clouds within the $n_0 = 10^7$ cm^{-3} solution achieve similar velocities only near the disk, but cannot match the increased terminal velocity in the $n_0 = 10^6$ cm^{-3} outflow. The $n_0 = 10^7$ cm^{-3} wind can achieve similar velocities near the disk due to higher density clouds. The clouds in this model have higher density because of the wind's higher density: the wind with greater density requires a higher magnetic field strength to launch the wind, which confines the clouds with higher density. The higher cloud density, in this case, results in an ionization parameter that is an order of magnitude lower, allowing normal continuum radiation driving to help drive the clouds to higher velocities.

The presence of clouds also explains another effect: close examination of Figure 8 shows an interesting near-correspondence of velocities for models with $n_0 = 10^7$ cm^{-3} and $n_0 = 10^9$ cm^{-3} toward the end of those outflows. For the lower density ($n_0 = 10^7$ cm^{-3}) wind, clouds push the wind to higher velocities. As the base wind density climbs to 10^8 cm^{-3} and 10^9 cm^{-3}, the clouds become less and less important, and continuum radiative driving primarily accelerates the continuous wind. The continuum driving dominates the wind briefly at the base of the wind, before the wind is overionized by the continuum, and then contributes again at larger distances when the clouds are much further from the central continuum and the ionization again drops with the decrease in incident flux. This effect leads to a delayed acceleration of the higher-density models relative to the lower-density models, whose lower-ionization clouds are accelerated by continuum radiative driving much closer to the disk, as can be seen in Figure 8.

The radiative acceleration of the continuous wind itself is also shown in Figure 9, where we present wind models with varying gas columns in front of the radiatively driven wind (the gas column shields the wind from too much ionizing radiation, allowing more efficient radiative acceleration; see MCGV95). The higher velocities attained by the radiatively driven winds relative to the pure-MHD wind are due to continuum radiative driving on the gas in the continuous wind itself. The clouds here are relatively unimportant. But this radiative acceleration is very dependent on density in the wind. When we examine the same variation in shielding but with a lower initial wind density in Figure 10, we see that radiative acceleration of the continuous wind is not important; the slight variations in the terminal velocity in Figure 10 are again due to clouds dragging the continuous wind as the clouds are accelerated radiatively.

Radiative acceleration can be important in the continuous wind in other circumstances, however: if we include dust within the continuous wind, this increases the continuous opacity and therefore the continuum radiative acceleration. In
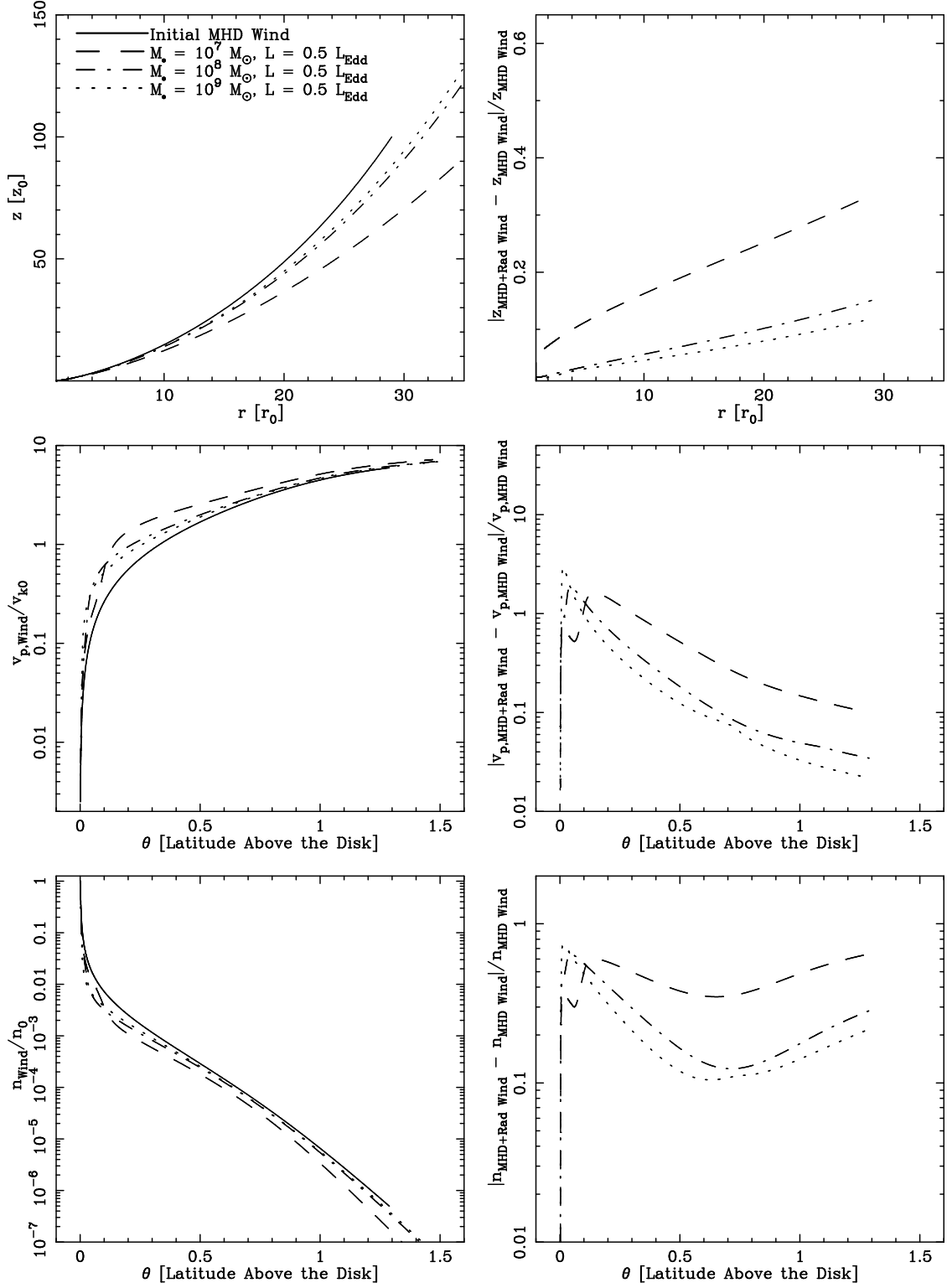
FIG. 17.— As in Fig. 6, but showing the variation in wind structure with changes in the mass of the central black hole.

the case of Figure 11, where we include dust in the continuous wind model, the radiative acceleration due to continuum opacity overwhelms the line driving by a factor of over 100. One can also see the domination of continuum driving in another way: winds of different density (compare the $n_0 = 10^8$ cm^{-3} to the $n_0 = 10^9$ cm^{-3} run in Fig. 11) have extremely similar structure and velocities when both winds include the same type of dust. [For both of these models, we have included ISM dust (Martin & Rouleau 1991; Mathis, Rumpl, & Nordsieck 1977) in the photoionization and radiative acceleration models.] Finally, it is very interesting to note that if we include a different kind of dust, such as Cloudy's Orion dust (Baldwin et al. 1991, see also §3.3.2), we see significantly different velocities (a 30% change in the terminal velocity of the wind with Orion dust versus a 20% change with ISM dust). This difference may be of use to researchers trying to gain a better understanding of AGN dust composition (e.g., Crenshaw et al. 2001).

In the remainder of our survey, radiative acceleration plays a key role in wind acceleration only very near the surface of the accretion disk, and has a much smaller role in determining the terminal velocities. The greatest changes in velocity near the accretion disk are exhibited for models with small amounts of gas shielding, such as those shown in Figure 9. In this figure, the chief culprit behind the large changes to velocity is continuum driving of the continuous wind. As the shielding in front of the wind is increased, the continuum flux drops, and so does the acceleration near the disk. Also, it is interesting to note that at these high densities and with clouds added into the continuous wind, the velocities are rather insensitive to the incident continuum, and show very much the same structure with either the MF87 or MCGV95 spectral energy distribution (see Fig. 12). However, the models do show a slight sensitivity to the incident spectrum for some values of the shielding column in front of the wind, as also displayed in Figure 12: the lower shielding allows for increased radiative acceleration nearer to the disk surface, resulting in higher continuum acceleration near the disk. The MF87 spectrum is slightly more effective in continuum acceleration, yielding the small difference in velocities between these two cases.

Large acceleration near the disk is also displayed in outflows where the wind is launched closer to the central black hole, as in Figure 13; this is simply due to the greater amount of flux at that smaller distance from the black hole. This flux primarily powers the acceleration of the wind through a short burst of continuum driving of the continuous wind as the outflow launches from the disk, before it is overionized by the intense radiation field. The higher density winds maintain lower ionization continuous winds further up in the flow, allowing more continuum acceleration, and accounting for the slightly larger terminal velocities in those cases.

The acceleration near the disk can also increase if the pure-MHD wind streamlines are less vertical and more radial (allowing radiative acceleration to work much more efficiently, since the radial direction is the direction in which photons are streaming in our model). This effect is displayed in Figure 14, where we vary κ, the dimensionless ratio of mass to magnetic flux in the wind. Higher values of κ result in streamlines that lift gas much more slowly from the disk's surface, and therefore are more radial. If we also vary κ as in Figure 14, but for a lower-density wind, radiative acceleration of the continuous wind is not as effective, and the acceleration of the wind near the disk is about an order of magnitude lower (see Fig. 16).

The above cases all show very high radiative acceleration near the accretion disk. An order of magnitude less acceleration near the disk is shown in many other models (see Figs. 16 – 17), although even this decreased force still results acceleration that is a factor of ~ 2 higher than in a pure centrifugally-driven wind. This variation of ~ 2 is very much like the the radiative acceleration of the fiducial $n_0 = 10^8$ cm^{-3}, $N_{\rm H} = 10^{25}$ cm^3 solution on which these models are based; the fact that these figures show relatively little perturbation from that previous model shows that the radiative acceleration is only weakly dependent on perturbations in these parameters. In all but the lowest-density cases, this added acceleration is fairly constant, even with changes in the central continuum. However, the acceleration does drop when the central luminosity decreases from the fiducial value of $0.5\,L_{\rm Edd}$ to $0.1\,L_{\rm Edd}$ (see Fig. 15).

In many of the above figures (e.g., Fig. 15) one may notice a slow oscillation in density with height above the disk. The large initial difference in density between the centrifugally driven wind and the radiatively modified wind is due to the acceleration of the wind close to the disk: because of mass conservation, radiative acceleration results in a large drop in the density compared to that in the pure MHD wind. Acceleration far from the disk causes the same effect. In both cases, we essentially witness the rise and fall of the ionization parameter, and with it, the corresponding decrease and increase of radiative acceleration. The large gas column near the surface of the disk leads to low ionization parameters there, allowing continuum radiative driving to dominate, accelerating the wind near the disk. As the wind climbs, the shield column drops, the ionization parameter increases, and radiative acceleration drops. As this magnetically collimated wind rises, it gradually climbs further and further away from the disk, and hence also from the central black hole; as the wind climbs, therefore, the flux striking the wind drops faster than the wind density, and the ionization parameter, U, again decreases. The lower ionization state leads to more lines for radiative acceleration, causing both line driving and continuum driving to increase, although continuum driving retains its dominance even far from the central source.

Before concluding this parameter survey, we briefly touch on the velocity differences predicted by this wind model when the mass of the central black hole is varied. These results are shown in Figure 17, which seems to present a rather paradoxical picture: as we increase $M_\bullet$ and the luminosity increases (since it is proportional to the Eddington value), the wind's structure, velocity, and density approach those of the initial, pure-MHD wind. In fact, the largest change in the streamlines, and largest change in the velocity, occur for the lowest mass black hole. This is due to our assumption that $L \propto L_{\rm Edd}$: for lower $M_\bullet$, this lower luminosity allows a lower ionization parameter in the continuous wind, which yields more continuum opacity in the wind, and hence larger continuum acceleration. Also, for the the case of $M_\bullet = 10^7 M_\odot$, the luminosity is low enough for dust to survive in the clouds, which further aids in the acceleration, although the continuum

driving of the wind is still the overriding source of acceleration.

5. CONCLUSIONS & FUTURE DIRECTIONS

We have presented a self-consistent, semianalytic, steady-state disk-wind model that combines magnetic and radiative accelerations and includes two gas phases: a magnetized continuous wind and embedded diamagnetic clouds. The continuous wind is driven centrifugally and, after rising above the disk surface, becomes subject to radiative acceleration by the central continuum source. The clouds are uplifted from the disk surface by the ram pressure of the continuous wind, which also confines them by its (largely magnetic) pressure, and they are subsequently pushed by the radiation pressure force of the central continuum. We calculate the radiative acceleration on both of those components from first principles, using detailed photoionization simulations to determine the ionization state of the gas and the continuum incident on that gas. Since the model includes magnetic launching, the outflow automatically incorporates a shielding column of gas that can attenuate the central continuum and allow efficient radiative acceleration in the outer parts of the wind. This addresses the problem of how to launch a shielding column in areas of the wind where radiative acceleration is not effective, because of the high degree of ionization of the gas.

We have used this model to illustrate the dependence of a two-phase magnetically and radiatively driven wind on various outflow parameters, and to demonstrate the care with which one must treat radiative acceleration calculations. We find that *the wind structure is significantly altered* when we include clouds that are also radiatively accelerated: their low filling factor, low ionization parameters, and the possibility of dust in the clouds all allow radiative acceleration when the continuous wind is too highly ionized for radiation to be an effective driving source. Not unexpectedly, clouds have the largest impact when their mass outflow rate is comparable to that of the wind itself. We have also determined that including dust in the continuous outflow can have a large impact on wind geometry and kinematics because of the increase in continuum opacity. Dust has a large enough impact on wind structure that even changing the type of dust results in significant changes in the outflow. Finally, we have found that higher-density winds with low shielding can be influenced heavily by radiative acceleration. In this case, radiative acceleration is not acting through the clouds but instead comes from the continuum driving in the continuous wind itself; large changes in the wind occur with dust present in the wind, but even the gas continuum opacity can result in large radiative acceleration of the continuous wind. This is a recurring theme in our results: continuum driving by and large plays a more important role in continuous wind acceleration than line driving. Line driving, on the other hand, is more important in the clouds.

We have also found that, in the context of our particular cloud model, much of the spectral dependence of radiative acceleration is largely erased, with different central continua producing very similar perturbations to the wind's structure and dynamics. Furthermore, we showed that variations in the mass of the central black hole and in the launching radius of the wind do not greatly modify the initial centrifugally-driven wind's structure or kinematics, although it is important to remember that changing both of these parameters affects the Keplerian velocity at the base of the wind, and hence changes the magnitude of the wind velocity.

Finally, we established that the velocity structure near the surface of the disk is very sensitive to radiative acceleration, which may be an important key to observationally distinguishing between pure MHD-driven winds and radiatively driven winds. While both accelerate rapidly from the disk, radiation pressure causes much greater initial acceleration as well as much larger drops in the density as the wind lifts off from the surface of the disk. This effect would be much more noticeable in AGNs with low shielding columns, where radiative acceleration is much stronger near the surface of the disk. As a result of mass conservation, the variations in density with altitude above the disk closely mirror those of the velocity, and may also be valuable tracers to discriminate between wind acceleration processes. This may hint that if Broad Emission Lines are formed near the disk surface, observations of those lines may be capable of distinguishing between different acceleration processes. It is important to note that we have not yet included the radiative acceleration due to intrinsic or reprocessed flux from the accretion disk itself as in MCGV95 and Proga et al. (2000). Including this effect may yield even stronger acceleration from the surface of the disk.

Our next step will be to fit this model to observations in an attempt to directly quantify the processes that act within AGN outflows. To complete this, it will be important to widen our parameter survey to include, for example, other incident spectra and dust compositions (to examine, for instance, the dust distribution found in Crenshaw et al. 2001). We are currently developing a Monte Carlo module that will allow both line emission and absorption predictions for a range of inclination angles. At the same time, we also hope to include the effect of radiation acceleration due to accretion disk flux and pursue observational signatures of embedded condensations that are not magnetically confined by the continuous wind (e.g., Bottorff & Ferland 2001). In addition, we can learn a great deal about the geometry of AGN outflows from polarization measurements (e.g., Corbett et al. 2000; Smith et al. 2002). The calculation of both line and continuum polarization will also be included in our Monte Carlo program. Finally, we note that this program is in no way restricted to considering AGN outflows alone; one can easily change the model's input parameters to study systems such as high-luminosity young stellar objects and cataclysmic variables, where similar outflows are observed.

6. ACKNOWLEDGEMENTS

APPENDIX

DERIVATION OF THE SELF-SIMILAR CENTRIFUGAL WIND EQUATIONS

In this appendix, we sketch the rederivation of our system of self-similar wind equations for the magneto-centrifugal wind structure. The equations utilized in this calculation advance upon those presented in BP82 and KK94: we consider not only a wind with arbitrary density power-law index, b, as in KK94, but also rederive the equations without the constraint of energy conservation. Since the radiation field continually inputs energy into the outflow, this is a very important modification, and was not fully considered within the derivation presented in KK94.

First, we work under the assumptions of stationary, axisymmetric, ideal, cold magnetohydrodynamic flow in cylindrical coordinates (r, ϕ, z). Our system of equations is based upon both the radial and vertical momentum equations:

$$v_r \frac{\partial v_r}{\partial r} + v_z \frac{\partial v_r}{\partial z} - \frac{v_\phi^2}{r} = -\rho \frac{\partial \Phi}{\partial r} - \frac{B_z}{4\pi} \left(\frac{\partial B_z}{\partial r} - \frac{\partial B_r}{\partial z} \right) - \frac{B_\phi}{4\pi r} \frac{\partial (r B_\phi)}{\partial r} \tag{A1}$$

$$\rho(\mathbf{v} \cdot \nabla) v_z = -\rho \frac{\partial \Phi}{\partial z} - \frac{1}{8\pi} \frac{\partial B^2}{\partial z} + \frac{1}{4\pi} (\mathbf{B} \cdot \nabla) B_z, \tag{A2}$$

$$\tag{A3}$$

where $\mathbf{v}$ is the fluid velocity, and $\mathbf{B}$ is the magnetic field strength. We neglect the thermal term, as we work in the zero-temperature limit. Φ is the effective gravitational potential, defined as

$$\Phi = -[1 - \Gamma(\theta)] \frac{GM_\bullet}{(r^2 + z^2)^{1/2}}, \tag{A4}$$

where $M_\bullet$ is the mass of the central black hole, and $\Gamma(\theta)$ gives the ratio radiative acceleration relative to the local gravitational field strength (see eq. 4).

We can solve these equations by first relating the flow velocity to the magnetic field via (see, e.g., Chandrasekhar 1956; Mestel 1961):

$$\mathbf{v}(\mathbf{r}) = \frac{k\mathbf{B}(\mathbf{r})}{4\pi\rho(\mathbf{r})} + (\omega(\mathbf{r}) \times \mathbf{r}), \tag{A5}$$

and stipulating mass conservation,

$$\nabla \cdot (\rho \mathbf{v}) = 0, \tag{A6}$$

where $k/4\pi$ is the ratio of mass flux to magnetic flux, and $\omega(\mathbf{r})$ and $\rho(\mathbf{r})$ are the angular velocity and mass density of the gas in the flow. Both the ω and k are conserved along magnetic field lines.

This system would normally have two integrals of motion: the specific energy and the specific angular momentum. However, since energy is continually added to the outflow, the specific energy is constant, and we can use only the specific angular momentum

$$l = r v_\phi - \frac{r B_\phi}{k}. \tag{A7}$$

We then impose self-similarity on this system by specifying

$$\mathbf{r} = [r_0 \xi(\chi), \phi, r_0 \chi] \tag{A8}$$
$$\mathbf{v} = [\xi'(\chi) f(\chi), g(\chi), f(\chi)] v_{K0}, \tag{A9}$$

where v_{K0} is the Keplerian velocity at the base of the outflow, $v_{K0} = (GM_\bullet/r)^{1/2}$, and the prime indicates differentiation with respect to χ. At the same time, we can re-express our constants in dimensionless form:

$$\lambda \equiv \frac{l}{(GM_\bullet r_0)^{1/2}} \tag{A10}$$

$$\kappa \equiv \frac{k(1 + \xi_0'^2)^{1/2}}{B_{p0}} v_{K0}, \tag{A11}$$

where B_{p0} is the initial poloidal magnetic field strength at the base of the wind.

As in KK94, we allow for a general power-law scaling of the density and magnetic field along the disk's surface:

$$\rho_0 \propto r_0^{-b} \tag{A12}$$

$$B_0 \propto r_0^{-(b+1)/2}. \tag{A13}$$

With this self-similar specification, the radial and vertical momentum equations become, after some simplification:

$$\frac{f\xi'm'}{\kappa\xi J} - \frac{f^2\xi'}{\xi J} + \xi''f^2 - \frac{(\lambda m - \xi^2)^2}{\xi^3(m-1)^2} = -\xi[1 - \Gamma(\theta)]S^3 - \frac{f}{\kappa\xi J^2}\left(\frac{-(1+\xi'^2)(b+1)}{2}+\right.$$
$$\frac{(\chi+\xi\xi')\xi'}{\xi} - \left.\frac{\xi''}{JS^2}\right) - \frac{\kappa f}{\xi}\frac{(\lambda-\xi^2)}{(m-1)}$$
$$\left[\frac{(\lambda-\xi^2)}{(m-1)}\frac{(-b+1)}{2} + \chi\left(\frac{2\xi\xi'}{(m-1)} + \frac{(\lambda-\xi^2)m'}{(m-1)^2}\right)\right] \tag{A14}$$

$$\frac{f}{\kappa\xi J}(m' - f\kappa\xi'J + f\kappa\xi\chi\xi'') = -[1-\Gamma(\theta)]\chi S^3 + \frac{f\xi'}{\kappa\xi J^2}\left(\frac{-(1+\xi'^2)(b+1)}{2}+\right.$$
$$\frac{(\chi+\xi\xi')\xi'}{\xi} - \left.\frac{\xi''(\chi^2+\xi^2)}{J}\right) -$$
$$\xi'\kappa f(\lambda-\xi^2)\left(\frac{(b+1)(\lambda-\xi^2)-2(\lambda+\xi^2)}{2\xi(m-1)^2}\right) +$$
$$\frac{(\lambda-\xi^2)^2 m'\kappa f}{(m-1)^3}. \tag{A15}$$

In the above, the following definitions are in play:

$$m = f\kappa\xi J = \frac{4\pi\rho v_p^2}{B_p^2} = \text{square of the Alfven Mach number} \tag{A16}$$

$$\Gamma(\theta) = \frac{a_{radiative}}{g} \tag{A17}$$

$$k/4\pi = \text{ratio of mass flux to magnetic flux (constant)} \tag{A18}$$

$$\kappa = \frac{k(1-\xi'^2_0)^{\frac{1}{2}}v_{k0}}{B_{p0}} = \text{dimensionless ratio of mass flux to magnetic flux} \tag{A19}$$

$$l = rv_\phi - \frac{rB_\phi}{k} = \text{specific angular momentum} \tag{A20}$$

$$\lambda = \frac{l}{(GMr_0)^{\frac{1}{2}}} = \text{normalized angular momentum} \tag{A21}$$

$$J = \xi - \chi\xi' \tag{A22}$$

$$S = 1/\sqrt{\xi^2 + \chi^2} \tag{A23}$$

$$\rho \propto R^{-b}. \tag{A24}$$

$$\tag{A25}$$

These two relations define the differential equations for m' and ξ'', which are, respectively, the spatial gradient in the poloidal Alfvén mach number (gradient with respect to height, χ) and the (cylindrical) radial velocity gradient (again with respect to χ).

One can see, from close inspection of the above equations, that many of the terms have a denominator of $(m-1)$, showing that when the gas crosses the Alfvén point (defined to be where $m = 1$), the equations become singular. The point $m = 1$ is therefore a critical point in the flow, where the downstream gas accelerates beyond the speed where upstream Alfvén waves can communicate with the rest of the wind. We can rewrite and solve the m' equation for the value of m' at the Alfvén point, with the result being

$$m'_A = 2\xi J[-8\chi\kappa^2\lambda m'\xi'J^3 + 4(1+b)\kappa^2\lambda\xi'^2J^2(\chi+\xi\xi') + m'^2(\chi+\xi\xi')(-2\kappa^2\lambda^2 S +$$
$$(1+b) + 2\kappa^2\lambda^3 - 4\chi\kappa^2\lambda^{\frac{3}{2}}(\lambda-S)\xi' + ((1+b) + 2\chi^2\kappa^2\lambda(\lambda-S))\xi'^2 +$$
$$2\kappa^2\lambda\Gamma(\theta)J^2)]/\left[4\xi J\left(\frac{4\kappa^2\lambda\xi'^2J^2}{S^2} + m'^2(\chi+\xi\xi')^2\right)\right]. \tag{A26}$$

We then use this constraint to our advantage, and start the integral at the Alfvén point with the value of m'_A given by Equation A26.

As covered in the main text, we then integrate these equations using a "shooting algorithm" to integrate both from the critical point and the disk surface, towards an intermediate point. Matching these two integrals at this common, central point allows us to solve for the three free parameters in our system, ξ'_0, ξ'_A, and χ_A.

CLOUD CALCULATION INITIAL CONDITIONS

For almost all cloud simulations, we use Cloudy to determine the internal cloud parameters. However, at the very base of the wind, Cloudy is very often unable to simulate the shielded, high density clouds, as almost all of the carbon within

the clouds becomes molecular. Therefore, we must define alternative approximations to the initial cloud parameters, which we do as follows:

$T_{Cloud,init}$: In our MHD wind models, we have already made the assumption that thermal driving (gas pressure) is unimportant. Physically, this means that the initial velocity of the wind (where we start tracking it) must be greater than or of order the local sound speed; otherwise, thermal effects can be communicated within the wind, and would then not be negligible, as we have assumed. We can use this assumption to estimate the temperature in the clouds. Basically, if we assume that the continuous wind velocity is of order of the sound speed in the wind, we can use that known initial wind velocity to estimate the temperature in the wind. We then approximate that the cloud temperature is of order the wind temperature at the disk's surface, which should be reasonable since the clouds form there. Thus, we can write

$$v_{wind,init} = c_s = \sqrt{\frac{k_B T_{wind,init}}{\mu m_p}} = \sqrt{\frac{k_B T_{cloud,init}}{\mu m_p}} \tag{B1}$$

$$\Rightarrow T_{cloud,init} = \frac{\mu m_p v_{wind,init}^2}{k_B}, \tag{B2}$$

where c_s is the speed of sound in the wind and μ is the mean particle mass in units of the mass of the proton, m_p. For gas near the disk, we set $\mu = 1$ for simplicity.

$n_{cloud,init}$: Having some idea of the initial temperature in the clouds, we now hypothesize (as we will throughout the model) that the clouds are in pressure equilibrium with the wind. For our model, the wind's pressure is dominated by the magnetic pressure. We are assuming that the clouds are diamagnetic so that $P_{mag} \ll P_{thermal}$; this also means that the clouds are not guided or accelerated by the magnetic field in the continuous wind. Since we already know the wind's magnetic pressure from the MHD calculations, we write

$$P_{wind} \approx P_{wind,mag} = P_{cloud} \tag{B3}$$

$$\Rightarrow n_{cloud,init} = \frac{P_{wind,mag}}{k_B T_{cloud,init}}. \tag{B4}$$

$R_{cloud,init}, M_{cloud,init}$: We solve for both of these simultaneously, given that each individual cloud mass, $M_{cloud,init}$, is some user-specified fraction of the maximum individual cloud mass that the wind could push up from of the disk by ram pressure ($M = \rho V$ where ρ is the mass density in the cloud and $V = \frac{4}{3}\pi R^3$ is the volume of the cloud; we assume spherical clouds for simplicity but admit that diamagnetic clouds may certainly be forced into other shapes). The equation for the maximum cloud mass is given by setting the ram pressure of the wind equal to the gravitational force on the cloud mass. In this case, for a mass rising up above the disk, the gravitational force to overcome is the tidal force, which is a fraction $\frac{h}{r}$ of the gravitational force due to the central source, where h is the scale height of the disk. Therefore, we write (as in Kartje, Königl, & Elitzur 1999)

$$\frac{GM_\bullet M_{cloud,max}}{r_{Launch}^2} \frac{h}{r} \approx C_F \pi R_{cloud,init}^2 \rho_{wind,init} v_{wind,init}^2 \tag{B5}$$

$$\Rightarrow M_{cloud,max} \approx \frac{C_F \pi R_{cloud,init}^2 \rho_{wind,init} v_{wind,init}^2 r_{Launch}^3}{GM_\bullet h}. \tag{B6}$$

But we also know that

$$M_{cloud} = \delta M_{cloud,max} = \frac{4}{3}\pi R_{cloud,init}^3 n_{cloud,init} m_p \tag{B7}$$

$$\Rightarrow M_{cloud,max} = \frac{4}{3\delta}\pi R_{cloud,init}^3 n_{cloud,init} m_p, \tag{B8}$$

where the user specifies δ. Setting the two expressions for $M_{cloud,max}$ equal, we can solve for $R_{cloud,init}$

$$R_{cloud,init} \approx \frac{3\delta}{4} \frac{C_F v_{wind,init}^2 r_{Launch}^3}{GM_\bullet h} \frac{n_{wind,init}}{n_{cloud,init}}. \tag{B9}$$

A useful approximation for thin accretion disks is that the ratio $\frac{h}{r} \approx \frac{c_s}{v_k}$ where c_s is the sound speed and v_k is the Keplerian velocity (we note that h obtained in this way is an upper limit if magnetic squeezing of the disk is important; see Wardle & Königl 1993). As already mentioned, very near the disk we assume that the wind is transonic, hence $v_{p,0} \geq c_s$. We therefore set $c_s \approx v_{p,0}$, since we know $v_{p,0}$ from the MHD calculations. Substituting this into our equation, and also setting $v_{wind,init}$ equal to the velocity at the base of the wind,

$$R_{cloud,init} \approx \frac{3\delta}{4} \frac{C_F v_{p,0} r_{Launch}^2 v_k}{GM_\bullet} \frac{n_{wind,init}}{n_{cloud,init}}. \tag{B10}$$

$$\tag{B11}$$

We use this equation to calculate the initial radius of the clouds that are launched into the wind.

$n_{cloud,ens}$: When we compute the interaction of the clouds with the wind, we need to know the ensemble density of clouds (i.e., the number density of clouds within the wind). We estimate $n_{cloud,ens}$ using the equation

$$\dot{M}_{cloud} = M_{cloud} n_{cloud,ens} v_{cloud} A \tag{B12}$$

$$\Rightarrow n_{cloud,ens} = \frac{\dot{M}_{cloud}}{M_{cloud} v_{cloud} A}, \tag{B13}$$

where $\dot{M}_{cloud}$ is the mass outflow rate due to clouds and A is the cross-sectional area of the outflow. At this stage of the flow, near the disk, we approximate $A = \pi(r_{outer}^2 - r_{inner}^2)$. Next, we define a user-specified parameter

$$\eta \equiv \frac{\dot{M}_{cloud}}{\dot{M}_{wind}}, \tag{B14}$$

which allows us to write

$$\Rightarrow n_{cloud,ens} = \frac{\eta \dot{M}_{wind}}{M_{cloud} v_{cloud} A}. \tag{B15}$$

The most important of the above parameters is the cloud mass, which requires an evaluation of all of the above parameters except for $n_{cloud,ens}$. Above the accretion disk, pressure equilibrium with the magnetic wind (determined through Cloudy) will set the density of a cloud, and since we already know the cloud mass, we can then calculate the radius of the cloud. This is necessary for computing the drag forces on the cloud (which scale as R_{cloud}^2).

Once all of the initial parameters have been found, we proceed to simulate clouds at any point in the flow.

<div align="center">REFERENCES</div>

Abbott, D.C. 1978, ApJ, 242, 1183

Antonucci, R. 1993, ARA&A, 31, 473

Arav, N., Li, Z., & Begelman, M.C. 1994, ApJ, 432, 62

Arav. N. 1996, ApJ, 465, 617

Arav, N., Barlow, T.A., Laor, A., & Blandford, R.D. 1997, MNRAS, 288, 1015

Arav, N., Barlow, T.A., Laor, A., Sargent, W.L.W, & Blandford, R.D. 1998, MNRAS, 297, 990

Axon, D.J. 2001, in ASP Conf. Ser. Vol. 249, The Central Kiloparsec of Starbursts and AGNs: The La Palma Connection, eds. Knapen, J.H., Beckman, J.E., Shlosman, I., & Mahoney,T.J. (San Francisco: ASP Press)

Baldwin, J., Ferland, G.J., Martin, P.G., Corbin, M., Cota, S., Peterson, B.M., & Slettebak, A., 1991, ApJ, 374, 580

Blandford, R.D., & Königl, A. 1979, Astrophys. Lett., 20, 15

Blandford, R.D., & Payne, D.G. 1982, MNRAS, 199, 883

Blandford, R.D. 2001, in PASP Conf. Ser. 224, "Probing the Physics of Active Galactic Nuclei by Multiwavelength Monitoring", ed. B. M. Peterson, R. S. Polidan & R. W. Pogge (San Francisco: PASP), 499

Bottorff, M., Korista, K.T., Shlosman, I., & Blandford, R.D. 1997, ApJ,479, 200

Bottorff, M., & Ferland, G. 2001, ApJ, 549, 118

Castor, J.I. 1970, MNRAS, 149, 111

Castor, J.I., Abbott, D.C., & Klein, R.I. 1976, ApJ, 195, 157

Chandrasekhar, S. 1956, ApJ, 124, 232

Chelouche, D., Netzer, H. 1999, MNRAS, 326, 916

Contopoulos, J., & Lovelace, R.V.E. 1994, ApJ, 429, 139

Corbett, E.A., Robinson, A., Axon, D.J., Young, S. 2000, MNRAS 319, 685

Crenshaw, D.M., Kraemer, S.B., Bruhweiler, F.C., Ruiz, J.R. 2001, ApJ, 555, 633

Dietrich, M., Wagner, S.J., Courvoisier, T. J.-L., Bock, H., & North, P. 1999, A&A, 351, 31

Draine B.T., & Lee, H.M. 1984, ApJ, 285, 89

Elvis, M. 2000, ApJ, 545, 63

Emmering, R.T., Blandford, R.D., & Shlosman, I. 1992, ApJ, 385, 460

Everett, J.E., Königl, A., Arav, N. 2002, ApJ, 569, 671

Ferland, G.J. 2002, Hazy, A Brief Introduction to Cloudy, University of Kentucky Department of Astronomy and Astrophysics Internal Report

Ganguly, R., Bond, N.A., Charlton, J.C., Eracleous, M., Brandt, W.N., & Churchill, C.W. 2001, ApJ, 549, 133

Hamann, F.W., Barlow, T.A., Chaffee, F.C., Foltz, C.B., & Weymann, R.J. 2001, ApJ, 550, 142

Kartje, J.F., Königl, A., & Elitzur, M. 1999, ApJ, 513, 180

Krolik, J.H. 1999, Active Galactic Nuclei: From the Central Black Hole to the Galactic Environment (Princeton: Princeton University Press)

Königl, A., & Kartje, J.F. 1994, ApJ, 434, 446

de Kool, M., & Begelman, M.C. 1995, ApJ, 455, 448

de Kool, M., Arav, N., Becker, R.H., Gregg, M.D., White, R.L., Laurent-Muehleisen, S.A., Price, T., & Korista, K.T. 2001, ApJ, 548, 609

Laor, A., & Brandt, W.N. 2002, ApJ, 569, 641

Livio, M. 1999, in "Probing the Physics of AGN by Multiwavelength Monitoring", eds. B.M. Peterson, R.S. Polidan, and R.W. Pogge, ASP Conference Series

Martin, P.G., & Rouleau, F. 1991, in Extreme Ultraviolet Astronomy, eds, Malina, R.F., Bowyer S., Pergamon Press, Oxford, 341

Mathews, W.G., & Ferland, G.J. 1987, ApJ, 323, 456

Mathis, J.S., Rumpl, W., & Nordsieck, K.H. 1977, ApJ, 217, 425

Mestel, L. 1961, MNRAS, 122, 473

Mihalas, D., & Weibel-Mihalas, B. 1999, Foundations of Radiation Hydrodynamics (New York: Dover)

Murray, N., & Chiang, J. 1997, ApJ, 474, 91

Murray, N., Chiang, J., Grossman, S.A., & Voit, G.M. 1995, ApJ,451, 498

Netzer, H. 1990, in Active Galactic Nuclei, Saas-Fee Advanced Course 20 (Berlin: Springer-Verlag), 57

Pappa, A., Georgantopolous, I., Stewart, G.C., & Zezas, A.L. 2001, MNRAS 326, 995

Peterson, B.M. 1997, An Introduction to Active Galactic Nuclei, (New York:Cambridge University Press)

Powell, M.J.D. 1970, in Numerical Methods for Nonlinear Algebraic Equations, ed. P. Rabinowitz (New York: Gordon and Breach).

Proga, D., Stone, J.M., & Kallman, T.R. 2000, ApJ, 543, 686

Proga, D., & Kallman, T.R 2002, ApJ, 565, 455

Proga, D. 2002, ApJ, in press (astro-ph/0210642)

Rees, M.J. 1987, MNRAS, 228, 47P

Safier, P. 1993, ApJ, 408, 115

Smith, J.E., Young, S., Robinson, A., Corbett, E.A., Giannuzzo, M.E., Axon, D.J., Hough, J. H. 2002, MNRAS, 335, 773

Sobolev, V.V. 1958 in Theoretical Astrophysics, ed. V.A. Ambartsumian (London: Pergamon)

Soboleb, V.V. 1960, Moving Envelopes of Stars (Cambridge: Harvard University Press)

Stevens, I.R, & Kallman, T.R., ApJ, 365, 321

Tielens, A.G.G.M., McKee, C.F., Seab, C.G., Hollenbach, D.J. 1994, ApJ, 431, 321

Urry, C.M., & Padovani, P. 1995, PASP, 107, 803

Verner, D.A., Verner, E.M., & Ferland, G.J. 1996, Atomic Data Nucl. Data Tables, 64, 1

Wardle, M., & Königl, A. 1993, ApJ, 410, 218

Weymann, R.J. 2002, in ASP Conf. Ser. Vol. 255, Mass Outflow in Active Galactic Nuclei: New Perspectives, eds. Crenshaw, D.M., Kraemer, S.B., and George, I.M. (San Francisco: ASP Press), 329